

Magnetostrictive Metal-Matrix Composites

Undergraduate Honors Thesis

Presented in Partial Fulfillment of the Requirements for

Graduation with Distinction at

The Ohio State University

By

Justin J. Scheidler,

* * * * *

The Ohio State University

2011

Examination Committee:

Dr. Marcelo Dapino, Adviser

Dr. Yann Guezennec

Approved by

Adviser

Graduate Program in
Mechanical Engineering

© Copyright by
Justin J. Scheidler
2011

ACKNOWLEDGMENTS

This research would not have been possible without the help of many individuals. First, I would like to express my gratitude to my research advisor, Dr. Marcelo Dapino, for giving me the opportunity to be a part of his exciting and ground-breaking research as an undergraduate. Also, insightful discussions with Professor Dapino were fundamental in my growth as a researcher and engineer. The time commitment and effort spent by Suryarghya Chakrabarti, Ryan Hahnen, Arjun Mahadevan, John Larson, and Paul Wolcott to ensure my understanding of concepts and provide assistance is greatly appreciated. To all of my colleagues in the Smart Materials and Structures Laboratory, I am thankful for your technical support and friendly discussions. I express my thanks to Professor Guezennec for serving on my committee. I am grateful for the expert insights from Eric Summers regarding Galfenol and its many complexities.

Outside of the lab, many friends and family helped make me who I am and have helped make my college career nearly stress free. To my friends: Ben, Drew, Alex, Stu, Steve, Patrick, Jake, David, Fahad, Tara, Amber, Allyn, Chelsea, Emily, and Alisha, thanks for all the memories. To my extended family, thank you for the support and laughter throughout the years. Special thanks to my girlfriend, Alyson, for always being there and being perfect in so many ways. Finally, nothing I have accomplished over the past 23 years would have been possible without the guidance of my parents,

Jeff and Nancy, or the help of my brother and sister, Josh and Nicole. I hope my actions and thoughts will reciprocate yours.

TABLE OF CONTENTS

	Page
Acknowledgments	ii
List of Tables	vi
List of Figures	vii
Chapters:	
1. Introduction	1
1.1 Background	1
1.2 Literature Review	5
1.2.1 Magnetic Principles	5
1.2.2 Magnetostrictive Principles	10
1.2.3 Galfenol	12
1.2.4 Ultrasonic Additive Manufacturing (UAM)	19
1.3 Objectives	25
2. UAM Embedding	26
2.1 Induction Coil Embedding	26
2.1.1 Composite and Embedded Materials	28
2.1.2 Build Preparation	28
2.1.3 UAM Process Parameters	29
2.1.4 Results	31
2.1.5 Analysis and Discussion	32
2.2 Iron-Gallium Embedding	34
2.2.1 Composite and Embedded Materials	35
2.2.2 UAM Process Parameters	37
2.2.3 Composite Development	37
2.2.4 Analysis and Discussion	43

3.	Magnetic Transduction Circuit	44
3.1	Design	44
3.1.1	Magnetic Flux-Linking Elements	44
3.1.2	Drive Coils	47
3.1.3	Material/Composite Characterization Setup	48
3.1.4	Cantilever Beam Vibration Setup	50
3.2	Manufacture of Components	51
3.2.1	Electrical Steel Laminates	53
3.2.2	Drive Coils	53
3.3	Verification and Modeling	55
3.3.1	Galfenol Material Model	55
3.3.2	Magnetic Circuit Design Verification	56
3.3.3	Composite Actuation Modeling	65
4.	Conclusion	71
	Bibliography	74

LIST OF TABLES

Table	Page
1.1 Magnetic material categorization by susceptibility	10
1.2 Mechanical properties of Galfenol alloys	15
2.1 Parameters for induction coil embeds	30
3.1 Critical buckling loads and maximum compressive stress that can be developed in Galfenol for testing of Galfenol sheets and Galfenol-Al composites	47
3.2 Solenoid constants used for finite element simulations	58
3.3 Mechanical and magnetic constants of electrical steel and Al 3003- H18 used for finite element simulations	60
3.4 Convergence of flux density in Galfenol	61

LIST OF FIGURES

Figure	Page
1.1 Body-centered cubic crystal structure and relevant crystallographic directions	13
1.2 “Goss” texture ($\{110\} \langle 001 \rangle$) shown on a BCC unit cell	14
1.3 Dependence of Magnetostriction on Ga content [65]	15
1.4 Characterization curves for highly textured, polycrystalline 18.4 <i>at%</i> Galfenol [45]	16
1.5 Magnetostriction as a function of the angle between $\langle 100 \rangle$ direction and rolling direction [47]	19
1.6 Schematic of UAM process	20
1.7 Optical micrograph of Al 3003–H18 manufactured using UAM, showing voids and bonded regions [30]	21
1.8 A: NiTi wire embedded into Al 3003–H18 using only plastic flow of Al sheet [28]. B: 3.175 mm wide, 25.4 μm thick PVDF ribbon wrapped with Kapton insulating tape and embedded into Al 3003 – H18 [29]. C: X-RAY of part shown in E, showing embedded channels (courtesy Edison Welding Institute). D: NiTi ribbon embedded into Al 3003 – H18 using only plastic flow of Al sheet [29]. E: bulk aluminum part with embedded channels (courtesy Edison Welding Institute). F: 381 μm NiTi wire embedded into Al 3003 – H18 using only plastic flow of Al sheet [27].	23
1.9 Very-high-power UAM system, with detail of ultrasonic stack (courtesy of Edison Welding Institute)	24

2.1	Induction coil build preparation	29
2.2	Insulation-stripped and deformed induction coil resulting from minimal Al bonding around coil (top Al foils manually peeled back for visualization of coil)	31
2.3	Weld interface of 30 turn induction coil build with no Kapton tape seams	33
2.4	Fully embedded 0.4 in wide steel specimen with wound 60 turn induction coil	33
2.5	Cross-section of the desired Galfenol-aluminum active composites . .	35
2.6	Fixture used to clamp welding plates to UAM machine: Al 3003-H18 plate bolted to steel base plate	36
2.7	EDM cut Galfenol steel build 3 (A) before and (B) after	38
2.8	Cross sectional view of rib deflection during the UAM process . . .	39
2.9	Before and after welding, and pressure film of rolled Galfenol steel UAM build 4	41
2.10	Post welding and pressure film of rolled Galfenol steel UAM build 5	41
3.1	Design of electrical steel laminates used to flux link composite to drive coils	46
3.2	Design of magnetic circuit for use with a load frame during characterization testing	49
3.3	Material/composite characterization setup	50
3.4	Design of cantilever beam vibration setup	51
3.5	Exploded view of aluminum fixturing used to cantilever composite to magnetic circuit and interface with a shaker	52
3.6	Cantilever beam vibration setup	52

3.7	Electrical steel laminate stacks; A and B used for material/composite characterization setup, A and C used for cantilever beam vibration setup	53
3.8	Machined block and fixture used to wind drive solenoids	54
3.9	Drive solenoids and relevant dimensions and properties	55
3.10	Simplified drive coils with current direction shown	57
3.11	Complexities of the magnetic transduction circuit retained for finite element modeling	58
3.12	Discretization of composite domains: (A) aluminum substrate, (B) Galfenol, (C) UAM aluminum foil	59
3.13	Mesh used to solve COMSOL simulations	61
3.14	Simulated magnetic flux path of the transduction circuit for different coil currents	63
3.15	Simulated magnetic flux distribution through the mid plane of the Galfenol thickness	64
3.16	Test magnetic circuit for actuation testing	65
3.17	Galfenol-aluminum composite created using UAM	66
3.18	Simulated vs. experimental actuation of FeGa-Al UAM composite .	66
3.19	Experimental actuation of FeGa-Al UAM composite [29]	68
3.20	Simulated strain in UAM composite due to the saturated Galfenol actuation at solenoids currents of 0.128 A	69

CHAPTER 1

INTRODUCTION

1.1 Background

The advent of smart materials, also known as adaptive or active materials, and their supporting research has led to an exciting and diverse array of new actuators, sensors, or self-sensing actuators. Smart materials have one or more properties, including shape, that exhibit controllable changes as a result of variable external inputs, such as stress, temperature, and magnetic fields to name a few. Along with the change in properties comes an inherent ability to convert energy from one form to another.

Smart materials have sparked the growing field of smart structures/systems, which focuses on combining active materials with support structures, electronics, and/or control systems to actively monitor changing environments and alter system properties or responses accordingly. One formal definition for a smart structure/system is a non-biological structure having a definite purpose, means and imperative to achieve that purpose, and a biological pattern of functioning [62].

The most well known and well researched smart materials are piezoceramics, electrostrictives, and shape memory alloys (SMA's). Piezoceramics develop a charge when stressed, which is based upon the piezoelectric effect. The benefits of piezoceramics

include being lightweight, compact, relatively inexpensive and having a nearly linear response when poled. Electrostrictives are governed by the inverse piezoelectric effect, whereby changes in electric field result in mechanical strain. Electrostrictive actuators, in general, have higher stiffness and increased strain compared to piezoelectric actuators for equal voltage inputs. However, their strain response is nonlinear. Shape memory alloys produce large strain without undergoing plastic deformation and can also recover this strain, due to phase changes within the material. Shape memory alloys have been found to sustain strains on the order of 8 % [46].

Magnetostrictives are another, less common smart material that experience mechanical deformations in response to changes in magnetic induction. While typically having lower coupling between the active domains and having significant frequency dependence, magnetostrictives retain many advantages over the more common smart materials presented above. Properties of piezoceramics and electrostrictives are irreversibly modified at elevated temperatures due to low Curie temperatures and phase transition temperatures. Thus, these materials are relegated to use in a temperature range around $60 - 90\text{ }^{\circ}\text{C}$ [44]. Temperature has a minimal effect on magnetostrictives below their Curie temperatures ($380\text{ }^{\circ}\text{C}$ or more [20]), and irreversible changes only occur near the melting point (about $1400\text{ }^{\circ}\text{C}$ [18]). In reference to SMA's, magnetostrictives have a much higher bandwidth ($\sim 30,000\text{ Hz}$ compared to $\sim 100\text{ Hz}$ [24]) and lower hysteresis. Further, magnetostrictive-based transducers have sustained more than 10^6 cycles without measurable change in output [3, 19]. The properties of piezoceramics and electrostrictives degrade over time due to depoling (which can be accelerated above normal levels due to overstress, overstrain, excessive voltage, or elevated temperatures). Similarly, the actuation response of Nitinol, the most common

shape memory alloy, significantly decreases for cycling above 10^4 cycles, with failure occurring at thousands of cycles for moderate bias stresses [4, 56].

Magnetostriction was first observed by James Joule in 1842, when he observed that iron sustained changes in length with the application of a magnetic field. Due to the very minimal strains (on the order of $10\ \mu\text{strain}$) seen in natural magnetostrictive materials, such as cobalt, nickel, and iron, magnetostrictives received little attention until 1963. In that year, the rare-earth element based material, Terfenol-D ($\text{Fe}_2\text{Tb}_{1/3}\text{Dy}_{2/3}$), was invented. With energy density and coupling factor comparable to piezoceramics and piezoelectrics, the capability to generate magnetostrictive stresses around 90 MPa, and strains upwards of 2000 ppm, Terfenol-D has received much attention and has developed into a viable smart material [20, 55, 77]. However, Terfenol-D is very brittle and is limited to applications that require only 1D loading of the material.

In 1999, the Magnetic Materials Group at Naval Surface Warfare Center, Carderock Division (NSWCCD) invented the magnetostrictive material, Galfenol (an acronym from **G**alium iron(**fe**) **N**aval **O**rdinance **L**aboratory). Galfenol has energy density and magnetomechanical coupling that are noticeably less than Terfenol-D. Despite, Galfenol can be machined, extruded, welded, rolled, deposited, and hot-formed, while also possessing structural properties. Namely, Galfenol can be subjected to compression, bending, shock/impact, and torsion. Additionally, Galfenol's magnetic response saturates around magnetic fields of only $4 - 6\ \text{kA/m}$, while Terfenol-D does not saturate until over $150\ \text{kA/m}$ (both at $\sim -7\ \text{MPa}$ bias stress) [19, 45]. Therefore, Galfenol is superior to Terfenol-D in applications where structural integrity/strength is required and/or magnetic field intensity for excitation is limited.

One challenge to designing smart structures and systems with Galfenol as the (or one of the) active element(s) is how to package or join the material to the rest of the system. Galfenol can be conventionally welded through fusion welding, however the material will recrystallize once below the melting temperature and domains will spontaneously form below the Curie temperature. This will remove all preprocessing of the material (grain structure, crystal structure alignment (texture), stress annealing, etc.) For Galfenol to be an effective active material, it would need to be reprocessed following fusion welding. Additional methods of producing smart structures that utilize Galfenol could include simply bonding Galfenol sheets to a surface, machining threads onto Galfenol rods allowing for conventional attachment, or even replacing the material of the structure with Galfenol itself. However, Galfenol is currently an expensive material, making it infeasible to employ in large volumes. Also, the most economical method of producing it will likely be rolling into sheets (not directional solidification into rods or related processes). Further, as Galfenol is largely iron-based, corrosion resistance is of great concern. One innovative method of incorporating Galfenol into structures that overcomes the complications stated above is a solid-state welding process, Ultrasonic Additive Manufacturing (UAM). As a solid-state process, UAM can produce coalescence of materials below their respective melting points. Thus, UAM offers the unique opportunity to embed temperature-sensitive materials into bulk substrates. UAM also has the benefit of welding dissimilar metals, allowing for Galfenol sheets to be embedded below corrosion resistant materials. With embedding of the material below the surface, opportunities to measure strains within a structure arise.

As a structural grade material, Galfenol structures manufactured with UAM are ideal for sensing applications in harsh environments, such as structural health monitoring in aircraft structures, where strict weight and size constraints limit sensor design. Also, considering the recent, high-profile oil spills, the maintenance and integrity of steel catenary risers (SCRs) on oil rigs is of great importance. In deep and ultra-deep sea drilling, extremely high pressure and elevated temperatures pose difficult technical challenges in catenary riser design and stress monitoring. Currently, SCR health monitoring is conducted through the use of external sensors measuring flex joint rotation and bending strain and stiffness [25, 43, 49, 68]. As the knowledge bases of UAM and Galfenol continue to grow, the possibility of using embedded Galfenol in these risers as concurrent structural members and internal sensors will become a reality.

1.2 Literature Review

1.2.1 Magnetic Principles

1.2.1.1 Magnetic Fields

Magnetic fields are generated whenever electrical charges move, whether in a current-carrying conductor or in the orbital motions and spins of electrons within an atom or atoms. When a magnetic field, \mathbf{H} , is produced in a volume of space, an energy gradient is developed within that volume, creating a force on electric charges, current-carrying conductors, and magnetic dipoles [31]. The Biot-Savart law, Equation (1.1), allows for calculation of the magnetic field strength produced by current through a given conductor,

$$\delta\mathbf{H} = \frac{1}{4\pi r^2} i * \delta\mathbf{l} \times \mathbf{u}, \quad (1.1)$$

where $\delta\mathbf{H}$ is the magnetic field increment due to the current element increment, $i\delta\mathbf{l}$, r is the distance from the current element to the point of interest, i is the current, $\delta\mathbf{l}$ is the incremental length of the conductor, and \mathbf{u} is a unit vector along r [31].

In order to increase the magnitude of the magnetic field generated, insulated wires are wound in a helical fashion to form solenoids. The field strength at the center of a long, thin solenoid ($L \gg D$) in air is determined from Ampere's law [31], Equation (1.2) (which can be shown equivalent to the Biot-Savart law),

$$\mathbf{H} = \frac{Ni}{L}, \quad (1.2)$$

where N is the number of helical turns of the conductor, L is the length of the solenoid, and D is the diameter of the solenoid. For thick solenoids of finite length, Equation (1.2) is no longer valid, and the corrected field strength at the center is given as Equation (1.3) [31],

$$\mathbf{H} = \frac{Ni}{a_1} \frac{F(\alpha, \beta)}{2\beta(\alpha - 1)}, \quad (1.3)$$

where

$$\alpha = \frac{a_2}{a_1} \quad (1.4)$$

$$\beta = \frac{L}{2a_1} \quad (1.5)$$

$$F(\alpha, \beta) = \beta[\operatorname{arcsinh}(\alpha/\beta) - \operatorname{arcsinh}(1/\beta)], \quad (1.6)$$

and a_1 is the radius of the innermost winding, and a_2 is the radius of the outermost winding.

The above relations for the field strength within solenoids are idealized. Errors arise when applying these concepts to actual solenoids, due to the packing factor of circular wires, imperfect winding, and the frequency dependence of current through

a wire for a given voltage. Additionally, the above relations are derived for steady currents, not time-varying currents¹. Further, the relations are inaccurate outside of the middle 50% of the length, with the magnetic field decreasing by a half at the end of the solenoid [31]. Despite these limitations, Equations (1.2) and (1.3) can be used for estimation purposes.

1.2.1.2 Magnetic Induction

Magnetic induction (\mathbf{B}), also known as flux density, is defined as the amount of magnetic flux through a surface of unit area. If a magnetic field is thought of as a vector field, where the spacing between vectors indicates the magnitude of field, then flux (ϕ), a scalar quantity, can be visualized as the *net* number of magnetic field lines passing through a surface. The quantitative relationship between magnetic induction, flux, and magnetic field is given in Equation (1.7),

$$\mathbf{B} = \frac{\phi}{A} = \mu \mathbf{H} = \mu_0 \mu_r \mathbf{H}, \quad (1.7)$$

where A is the area over which the flux penetrates, μ is the permeability, μ_0 is the permeability of free space ($4\pi 10^{-7}$ in SI units), and μ_r is the relative permeability. Relative permeability is a material property that is equal to 1 (by definition) for free space, is nearly constant over large ranges of \mathbf{H} for paramagnetic and diamagnetic materials, and is nonlinear for ferromagnetic materials.

According to Gauss's law for magnetic fields², the *total* magnetic flux through *any closed* surface is zero (no magnetic monopoles exist in nature that would create magnetic field sinks or sources). Thus, magnetic field lines, and therefore magnetic

¹The 4th of Maxwell's equations, or the Ampere-Maxwell law, handles time-varying currents [23]

²Also considered as the second of Maxwell's equations

induction, must form closed loops with no distinct beginning or end. Gauss's law for magnetic fields is given as Equation (1.8)[23] (for the differential form, which is most common),

$$\vec{\nabla} \bullet \vec{\mathbf{B}} = 0. \quad (1.8)$$

In Equation (1.8), $\vec{\nabla}$ is the divergence operator. When ferromagnetic materials are placed in close proximity to magnetic fields, these loops of magnetic flux tend to concentrate in the ferromagnetic materials, due to their high relative permeabilities. As these ferromagnetic materials are connected by the loops of magnetic flux, they are said to be flux-linked. This allows for the components in a flux-linked loop to be magnetized by magnetizing just one of the components.

From Equations (1.7) and (1.1), it can be seen that current-carrying conductors produce magnetic fields, and consequently magnetic flux through the surrounding medium. The reverse process of a magnetic flux inducing voltage in a conductor can also be observed, and is governed by Faraday's law³ (given in differential form, as is most common), Equation (1.9) [23],

$$\vec{\nabla} \times \vec{\mathbf{E}} = -\frac{\partial \vec{\mathbf{B}}}{\partial t}, \quad (1.9)$$

where $\vec{\mathbf{E}}$ is the electric field, and $\vec{\nabla} \times$ is the curl operator. Faraday's law indicates that when a changing magnetic flux (produced from time-varying magnetic fields or motion of a permanent magnet through said surface) penetrates a surface, an electric field⁴ is induced along the boundary of the surface. When a conducting medium is present along the boundary, this electric field provides an electromotive force (emf).

³Also considered as the third of Maxwell's equations

⁴With a divergence of zero, meaning that the electric field lines circulate back on themselves. This is different from electric fields generated by electric charges, which have a nonzero divergence

The emf acts as a voltage⁵ to produce current within the conducting medium. Further, the negative sign on the right hand side of Equation (1.9) indicates that the induced current creates its own magnetic field that *opposes* the change in flux through the surface. Faraday's law is the foundation for the development of induction coils, which are widely used to measure magnetic induction or flux through surfaces. Numerous induction coils have arose for a variety of applications [69].

1.2.1.3 Magnetization

The most elementary unit of magnetism is considered as a single current loop⁶. From this, the magnetic dipole moment, \mathbf{m} can be defined using Equation (1.10) [31],

$$\mathbf{m} = Ai, \quad (1.10)$$

where A is the area of the current loop. Using the magnetic moment, \mathbf{m} , the magnetization, \mathbf{M} , can be defined as the number of magnetic dipole moments per unit volume pointing in a particular direction, as seen in Equation (1.11) [31],

$$\mathbf{M} = \frac{\mathbf{m}}{V}. \quad (1.11)$$

Since magnetic induction creates a torque on magnetic dipoles of moment, \mathbf{m} , the magnetic induction can therefore be related to magnetization, by Equation (1.12). Thus, magnetic flux densities can be generated by conventional currents (by magnetic fields) or by groups of magnetic dipole moments (by magnetization), shown in Equation (1.13) [31],

$$\mathbf{B} = \mu_0 \mathbf{M}, \quad (1.12)$$

⁵Not a force

⁶Which can be conventional current flowing in a conductor, unbalanced orbital motion of electrons about a nucleus within a material, or spinning of unpaired electrons within a material

$$\mathbf{B} = \mu_0(\mathbf{H} + \mathbf{M}). \quad (1.13)$$

An additional property of magnetic materials can now be introduced. The susceptibility, (χ) , is defined in Equation (1.14) [31],

$$\chi = \frac{\mathbf{M}}{\mathbf{H}}. \quad (1.14)$$

Magnetic materials are typically categorized according to susceptibility, as shown in Table 1.1 [31].

Table 1.1: Magnetic material categorization by susceptibility

Material Category	Susceptibility
diamagnetic	$\approx -10^{-5}$
paramagnetic	$\approx 10^{-3}$ to 10^{-5}
ferromagnetic	≈ 50 to $10,000$

1.2.2 Magnetostrictive Principles

For almost all ferromagnetic materials, dimension changes of the materials occur when they become magnetized, thereby creating a coupling of the magnetic and mechanical states of these materials. The strain developed in magnetostrictive materials in response to a magnetization change is known as magnetostriction⁷, (λ) , and arises due to the presence of magnetic domains. Magnetic domains are localized groups of material unit cells that have an ordered orientation, meaning that their magnetic moments all point in the same direction. As these magnetic moments, or dipoles, rotate into the direction of the applied magnetic field, the atomic spacing

⁷This is more formally called the Joule or direct effect

of iron and gallium atoms changes, leading to a deformation of the crystal structure. Typically, these magnetic domains are composed of $10^{12} - 10^{15}$ atoms [31]. In all ferromagnetic materials, magnetic domains form spontaneously below the material's respective Curie temperature. This formation of domains causes a spontaneous magnetostriction of the material as it cools through its Curie temperature. Further magnetostriction, known as field-induced magnetostriction, results from applied magnetic fields, which tend to rotate all of the domains within a material into the direction of the applied field. When all of the domains within a sample are aligned along the field direction, creating a single-domained sample, the sample is said to be technically saturated. The saturation magnetostriction, or λ_s , is the total strain developed by the spontaneous magnetostriction and the field-induced magnetostriction at technical saturation. Prior to the saturation region, the magnetostriction has a quadratic dependence on applied magnetic field.

The inverse Joule effect, also known as the Villari effect or simply the inverse effect, can also be observed in nearly all ferromagnetic materials. This is defined as the change in magnetization that occurs as a result of changes in stress. The Joule and Villari effects are the most common magnetostrictive effects, but a number of others exist⁸.

These effects are nonlinear and also depend on material history⁹. The nonlinearities arise from the saturation phenomenon seen in both magnetostriction and magnetization, as discussed above, and material anisotropies. These anisotropies are the

⁸See [12]

⁹Hysteresis is observed in magnetic and mechanical responses

domain-scale texturing¹⁰ and the atomic-scale preferred crystallographic directions. The preferred crystalline directions are defined as the directions that a magnetic moment tends to point due to an electrical attraction or repulsion between its rigidly attached electronic charge cloud and the neighboring charged ions [17]. Since each magnetostrictive material has a specific atomic structure¹¹ and electronic charge cloud configuration, they each may have different preferred crystalline directions.

To deal with these nonlinearities, the coupled linear piezomagnetic equations, Equations (1.15) and (1.16), were developed [8],

$$\mathbf{B} = d^*\mathbf{T} + \mu^{\mathbf{T}}\mathbf{H}, \quad (1.15)$$

$$\mathbf{S} = \frac{1}{E_y^{\mathbf{H}}}\mathbf{T} + d\mathbf{H}, \quad (1.16)$$

where \mathbf{S} is the strain vector, \mathbf{T} is the stress vector, \mathbf{B} is the flux density vector, \mathbf{H} is the magnetic field vector, $\mu^{\mathbf{T}}$ is the tensor of magnetic permeability at constant stress, $E_y^{\mathbf{H}}$ is the tensor of Young's modulus at constant magnetic field, d is the magnetomechanical strain tensor, and d^* is a magnetomechanical tensor. These equations are useful to describe small-signal operation about a bias stress or magnetic field, or for modeling to computationally calculate strain or flux density through iterative techniques.

1.2.3 Galfenol

1.2.3.1 Binary Galfenol ($\text{Fe}_{100-x}\text{Ga}_x$)

Binary Galfenol has a body-centered cubic crystal structure. In Galfenol, the crystalline direction in which the magnetic moments tend to prefer (or the magnetic

¹⁰Material processing that results in a significant majority of crystals in the material oriented in a specified direction

¹¹FCC, BCC, HCP, etc.

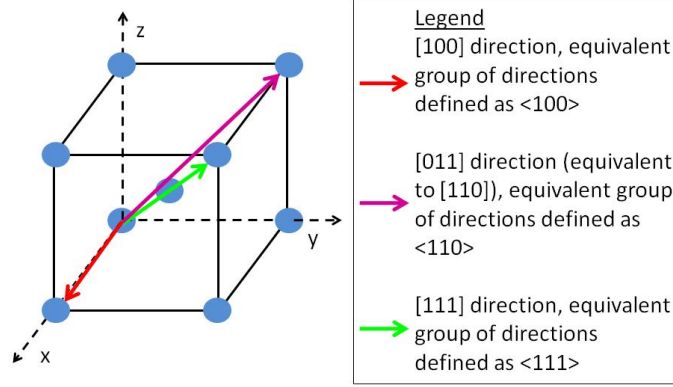


Figure 1.1: Body-centered cubic crystal structure and relevant crystallographic directions

“easy” axis) is the $\langle 100 \rangle$ family of directions. Thus, the achievement of an ideal Galfenol actuator or sensor relies on developing a strong $\langle 100 \rangle$ crystal orientation along the axis of elongation or sensitivity. In iron, and therefore Galfenol, the directions $\langle 110 \rangle$ and $\langle 111 \rangle$ are known as the “medium” and “hard” magnetic axes, respectively [75]. These directions are shown on a generic body-centered cubic unit cell in Figure 1.1.

Achievement of the desired orientation is conducted through texturing. Effects of texturing and efforts to produce said texturing via alloying additions and material processing have been studied [7, 35, 52, 67]. One promising method is to develop a “Goss” texture (defined as $\{110\} \langle 001 \rangle$) along the desired actuation direction (normally parallel to the rolling direction). The “Goss” texture direction is shown on a BCC unit cell in Figure 1.2. Therefore, in order to yield the maximum actuation along the rolling direction of a sample, it is necessary to orient the crystal structure such that the purple plane, shown in Figure 1.2, is coincident with the rolling plane and the red arrow is coincident with the desired actuation direction. This will orient

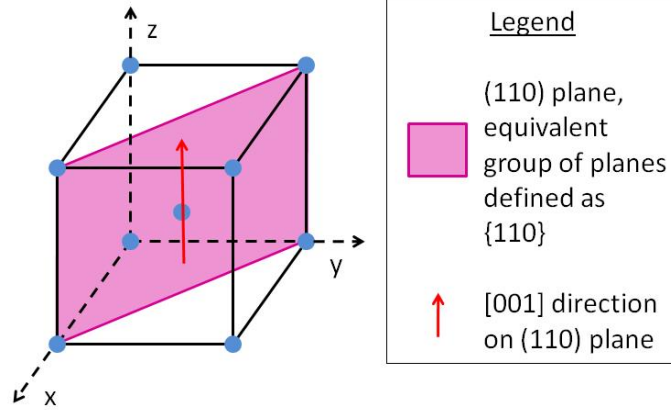


Figure 1.2: “Goss” texture ($\{110\} \langle 001 \rangle$) shown on a BCC unit cell

the crystal structure such that one of the magnetic “easy” axes is coincident with the rolling or actuation direction, and will result in the magnetic domains being oriented equally along the $[001]$ direction and each of the equivalent directions.

Single crystal samples of Galfenol result in the highest magnetomechanical response. However, polycrystalline samples are less expensive to produce and have mechanical properties that are superior to the single crystals. For maximum magnetostrictive performance in polycrystals, the highest possible volume fraction of $\langle 100 \rangle$ oriented crystal grains is desired.

Another variable that has a significant effect on the magnetostrictive performance of Galfenol is the composition of gallium. The effect of this composition on magnetostriction in single crystals was first described in 2003 [10], and later updated in 2007 [65], with the latter shown in Figure 1.3¹² (where Q indicates water quenched from 1000 °C, and SC indicates slow-cooled at 10 °C/min from 1000 °C). Explanations for this dependence and its curve have been formulated [72].

¹²Published in [65], taken from [72]

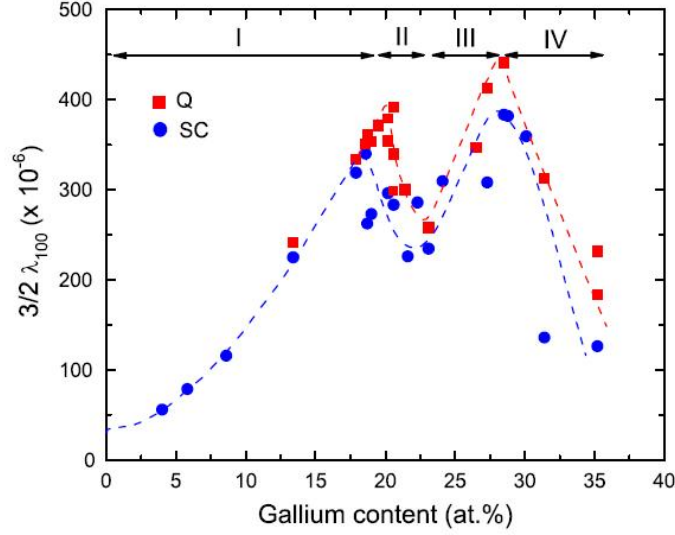


Figure 1.3: Dependence of Magnetostriction on Ga content [65]

Temperature has been shown to have minimal effect on the magnetostriction, magnetization, and elastic properties of Galfenol [9, 34, 58]. For various compositions and processing conditions, the mechanical properties shown in Table 1.2 have been found [64].

Table 1.2: Mechanical properties of Galfenol alloys

Property	Range
Ultimate Tensile Strength (UTS)	350 – 580 Mpa
% Elongation	0.8 – 1.6 %
Elastic Modulus	72 – 86 Gpa

From Equations (1.15) and (1.16), it can be seen that the determination of four quantities (μ^T , E_y^H , d , and d^*) characterize magnetostrictive materials. Therefore, four graphs, showing how these four quantities change in response to magnetic or

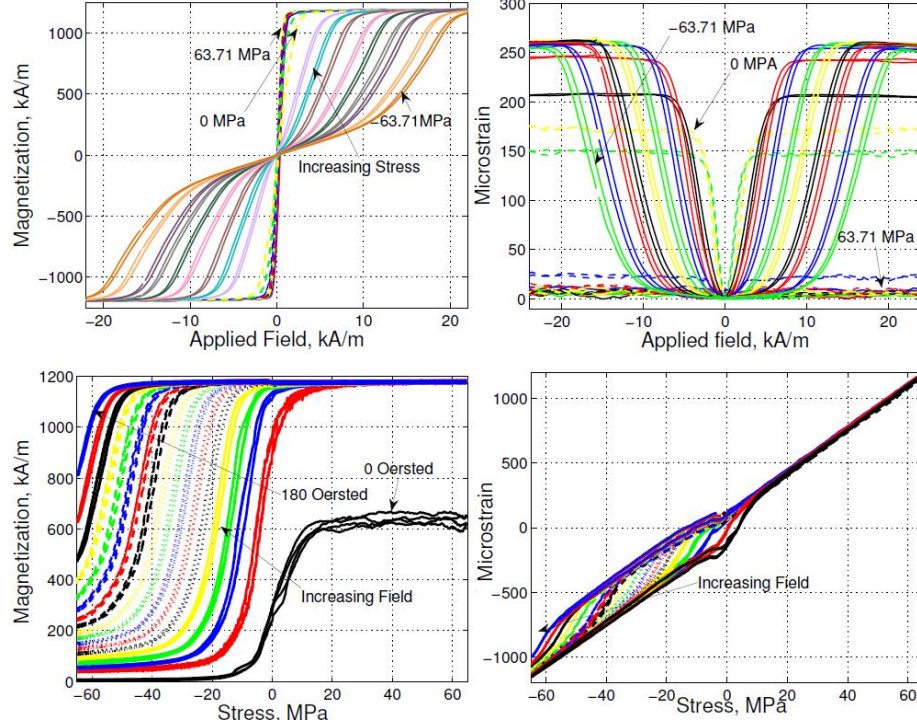


Figure 1.4: Characterization curves for highly textured, polycrystalline 18.4 *at%* Galfenol [45]

mechanical inputs, can define the transduction and sensing response of magnetostrictives, such as Galfenol. As an example, these four characteristic curves for a highly textured, polycrystalline rod of Galfenol (with 18.4 *at%* Ga) has been reproduced here in Figure 1.4 from [45].

In order to obtain the maximum performance from a Galfenol-based actuator, large compressive pre-stresses are required. To reduce or eliminate this need, stress annealing [71, 70] or magnetic field annealing [74, 75, 73] can be utilized during materials processing.

Notable modeling efforts include the Armstrong model [2] and the Evans-Dapino models. The Armstrong model is an anhysteretic model for magnetostrictives with

cubic anisotropy that calculates magnetization and magnetostriction. This model includes the effects of stress and anisotropy. Evans and Dapino have developed models for both 3D constitutive behavior of Galfenol [21] and system-level dynamic behavior of Galfenol-driven systems [22].

1.2.3.2 Rolled Galfenol

For many applications, including the production of Galfenol-based composites, the Galfenol material will need to be laminated or produced in thin sheets. This is a necessity due to the material’s high magnetic permeability, which causes large eddy current losses during dynamic operation. Also, rolled Galfenol sheet will likely be the most economical method of manufacture. Further, the embedding or incorporation of Galfenol into active structures often requires sheet geometries. Rolling of iron-gallium alloys was first attempted as recently as 2003 [35, 33].

The magnitude of the magnetomechanical response of rolled Galfenol still depends upon the material having a strong $\langle 100 \rangle$ orientation along the desired actuation direction. Additionally, finite element simulations have shown that mismatches in grain orientation can produce significant internal stresses, which lead to reductions in magnetostrictive response [35]. It has been concluded that this texturing cannot be achieved without the use of alloying additions¹³ [47]. Various attempts have been made to develop the desired $\langle 100 \rangle$ texture, through the use of alloying additions of silicon and boron [51], NbC [63], and low carbon steel [66].

While gallium is necessary for improving the magnetostriction of iron by twenty fold or more, it also has an embrittling effect on iron. Thus, initial attempts at rolling the binary Galfenol resulted in significant edge cracking, even during 1000 °C hot

¹³these are second-phase particles that inhibit the growth of grains with undesired orientation

rolling [53]. To improve rollability and ductility, Mo, Nb, NbC, B, and low carbon steel additions have been shown to produce adequate to high-quality rolled sheets [53, 64, 66]. Additionally, it has been shown that low carbon steel-based alloys of Galfenol experience a ductile to brittle transition between 15.5 at% and 18.4 at% Ga [64]. In this research, Galfenol samples with a nominal gallium content of 18.4 at% were chosen to balance the effect of gallium content on magnetostrictive performance (as shown in Figure 1.3) with the embrittling effect of increasing gallium content.

The largest magnetostrictions for rolled Galfenol samples to date have been reported by Meloy and Summers for Fe-Ga₁₈-NbC¹⁴ with a magnitude of 310 ppm. They also developed a plot showing magnetostriction as a function of texture orientation, reproduced in Figure 1.5 [47]. In Figure 1.5, the majority of grains in all samples were oriented in the $\langle 100 \rangle$ direction, but the $\langle 100 \rangle$ direction deviated from the rolling direction by $0 - 45^\circ$ ¹⁵. Also, the dotted line is a Gaussian trend line, while the solid lines are a 95% confidence range.

A magnetomechanical plate model has been developed to predict the nonlinear actuation response of laminated structures composed of magnetostrictives and non-magnetic layers [14]. This model was formulated based upon classical laminated plate theory and an energy-based statistical magnetomechanical model. A non-linear magnetomechanical plate model has also been developed to predict the effect of quasi-static stress and the magnetic field on the magnetic induction, elastic and magnetostrictive strain, and stress in laminated structures composed of magnetostrictive

¹⁴processing details provided in [47]

¹⁵recall that the magnetic “easy” axis is the $\langle 100 \rangle$ direction, which should be oriented parallel to the actuation direction for maximum magnetostrictive performance

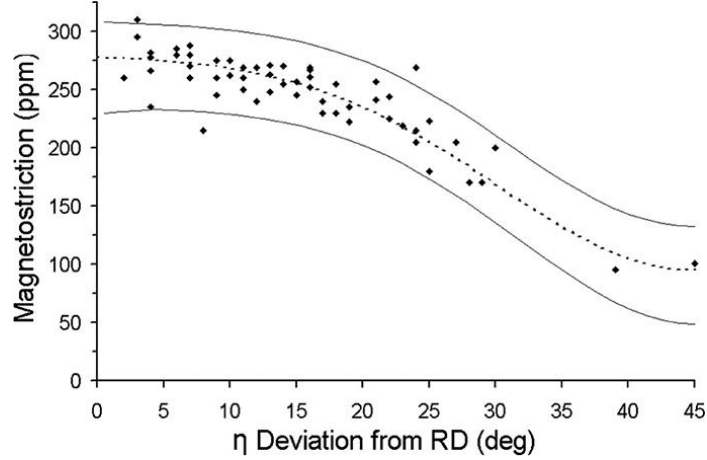


Figure 1.5: Magnetostriction as a function of the angle between $\langle 100 \rangle$ direction and rolling direction [47]

and non-magnetic components [13]. This model was formulated using the same techniques used for the actuation model described above.

1.2.4 Ultrasonic Additive Manufacturing (UAM)

Ultrasonic Additive Manufacturing (UAM), also known as Ultrasonic Consolidation (UC), is a groundbreaking solid-state welding process incorporating ultrasonic welding, additive manufacturing/rapid prototyping, and computer-aided machining (CAM) components. A schematic of the process is shown in Figure 1.6. The barriers to solid-state welding are asperities, oxides, and surface contamination. In UAM, ultrasonic vibrations, along with significant normal forces (upwards of 4500 N), are applied to induce plastic deformation and shearing of asperities, while dispersing

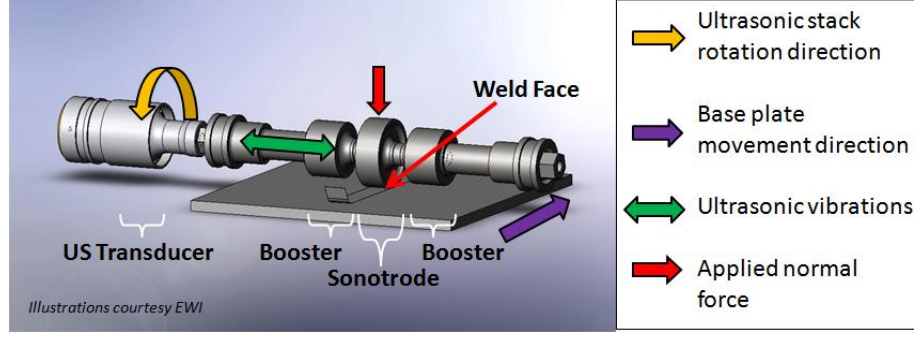


Figure 1.6: Schematic of UAM process (photograph courtesy of Edison Welding Institute)

oxides and contaminants [15]. With these barriers to welding eliminated or significantly reduced, nascent surfaces are formed and spontaneous metal to metal bonding occurs¹⁶.

The ultrasonic vibrations are delivered via piezoelectric-based transducers. High-powered UAM systems have ultrasonic powers of 9.5 kW, achieved by utilizing two transducers¹⁷. While the ultrasonic vibrations and normal force are applied, the ultrasonic stack (including the transducer(s), boosters, and sonotrode) is rotated and the base plate is translated in a coordinated way such that the sonotrode, or welding horn, traverses along the length of the weld. Vibration amplitudes range from 0.00019 – 0.0019 in ($5 - 50 \mu\text{m}$), with translation or travel speeds reaching 2 in/s ($\sim 50 \text{ mm/s}$) [16].

During each welding pass, thin metal sheets (0.006 in or $\sim 0.15 \text{ mm}$ thick) are welded to a base plate or to previously welded sheets. In the case of welding on top

¹⁶this results if the surface energies of the free surfaces are greater than the surface energy of the grain boundary between the two bonded metals

¹⁷where the two transducers and two boosters are symmetric about the sonotrode

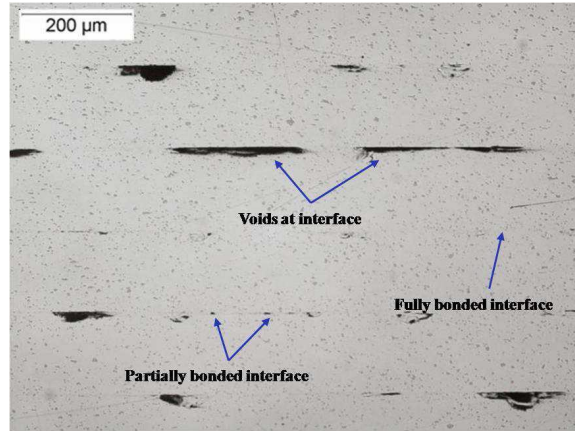


Figure 1.7: Optical micrograph of Al 3003 – H18 manufactured using UAM, showing voids and bonded regions [30]

of previously welded sheets, the sonotrode texture is imparted onto the top of the previously welded sheet, which becomes the bottom surface of the welding interface. Thus, the bottom of each welding interface is textured, while the top is the smooth rolled surface of a new sheet. It has been suggested that this situation is the cause for the residual voids that occur throughout the welded interface [32]. These voids are shown in Figure 1.7, taken from [30]. These voids are significantly reduced in size and number or even eliminated as vibration amplitude increases, travel speed decreases, and/or normal force increases. The effect of sonotrode texture on parts made using UAM has been reported in [42].

It was initially thought that the fewer number of voids the higher the strength and weld quality. However, a recent study has shown that the USS and UTTS of UAM built Al 3003 – H18 samples was not directly correlated with linear weld density (LWD) [30]. LWD is defined as the ratio of microscopically observed “bonded” regions to “unbonded” regions at the welding interface, and is reported as an averaged percent

[30]. Thus, further studies on the strength of UAM builds and their fatigue properties are needed.

As ultrasonic consolidation is a new process, most of the literature has focused on the development of optimum process parameters. The parameters that are typically studied include vibration amplitude, normal force, travel speed, and in some cases preheat temperature or number of bilayers (tapes welded during one welding pass). A selection of notable studies are [30, 38, 39, 40, 41, 57].

During the UAM process, temperatures only reach 30 – 50 % of the melting temperature of the base metal [39]. Further, the CAM component of the UAM process allows for complex internal channels and geometries. Together, the low-temperatures and complex internal geometries provide the unprecedented opportunity to embed temperature-sensitive materials, such as shape-memory alloys and other smart materials, to create active composites and structures. A variety of successful embeds are shown in Figure 1.8 [28, 29, 27].

The range of applications are broad, extending to the welding of dissimilar metals, welding of “hard” metals (such as Ti, Cu, Ni, and stainless steel) [54], parts with embedded sensing [50], and parts with motion, stiffness, or temperature control to name a few [26].

1.2.4.1 Very-High-Power UAM System

All embedding trials reported throughout this research were performed on a recently developed very-high-power UAM (VHP UAM) “test bed” as reported in [54]. This UAM system has 9 kW of power due to the use of two ultrasonic transducers (each with 4.5 kW of power) operating in unison using a push-pull method. The VHP UAM system is shown in Figure 1.9.

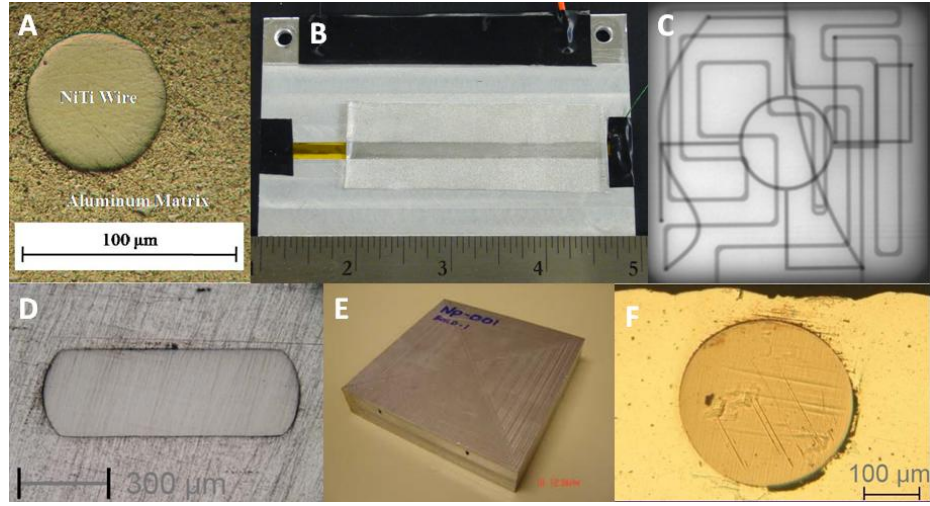


Figure 1.8: A: NiTi wire embedded into Al 3003 – H18 using only plastic flow of Al sheet [28]. B: 3.175 mm wide, 25.4 μm thick PVDF ribbon wrapped with Kapton insulating tape and embedded into Al 3003 – H18 [29]. C: X-RAY of part shown in E, showing embedded channels (courtesy Edison Welding Institute). D: NiTi ribbon embedded into Al 3003–H18 using only plastic flow of Al sheet [29]. E: bulk aluminum part with embedded channels (courtesy Edison Welding Institute). F: 381 μm NiTi wire embedded into Al 3003 – H18 using only plastic flow of Al sheet [27].

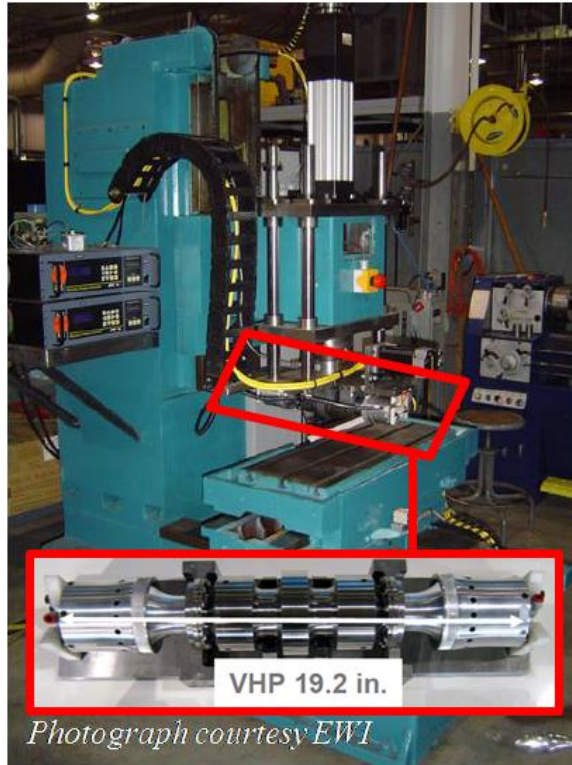


Figure 1.9: Very-high-power UAM system, with detail of ultrasonic stack (courtesy of Edison Welding Institute)

The system is tuned to operate at 20 kHz, and can provide normal forces up to 15 kN and vibration amplitudes up to 52 μm [61]. The sonotrode used with this system has a typical surface roughness of 7 μm Ra.

1.3 Objectives

The main objective of this research is to design, model, and build a magnetic transduction circuit intended to measure the sensing response to bending of Galfenol-aluminum composites created using UAM. As rolled Galfenol materials have only been studied as recently as 2003, little experimental data exists, with most studies focusing on magnetostriction. Therefore, the magnetic transduction circuit was also designed to characterize thin sheet rolled Galfenol using standard tension/compression load frames. COMSOL multiphysics with Matlab was used to model the magnetic characteristics of the transduction circuit to verify its design and predict any limitations to its use. The simulation was also utilized to predict the actuation response of the UAM composites, by incorporating a fully-coupled, piecewise-linear constitutive model of Galfenol that has been shown to accurately model magnetostrictive transducers [6, 22]. Experimental actuation data for a Galfenol-aluminum composite (prepared by [29]) was compared to a simulated response.

In an effort to develop a self-contained, Galfenol-based sensor/energy harvester, steel sheets wound with induction coils were embedded via ultrasonic additive manufacturing. This work tested the viability of the UAM process to concurrently embed active materials and sensitive electronic circuitry. Prior research on the embedding of Galfenol steel into aluminum substrates using UAM [29] was continued to include the embedding of rolled Galfenol steel. Great promise in this area has been shown.

CHAPTER 2

UAM EMBEDDING

2.1 Induction Coil Embedding

Previous research has shown that wires of up to 381 μm [27], including Fiber Bragg Grating (FBG) arrays [50], 250 μm optical fibers [37], and USB-based electrical systems [60] have been successfully embedded using the ultrasonic consolidation process.

In [37, 50], it was shown that sufficient plastic flow occurred to encapsulate and embed said fibers into an Al 3003-H18 matrix, without damaging the embedded materials. Each researcher followed a process very similar to these steps: (1) monolithic Al foils were formed by consolidating groups of two Al foils (typically 100 μm each, totaling 200 μm) (2) embedded elements were sandwiched between monolithic Al foils (3) the sandwich was clamped and welded along the length by UAM. In [27], a similar process was followed, except the two Al foils were not preformed into a monolithic foil.

The USB-based electrical systems were embedded by machining a sizable pocket into a bulk UC build, bonding the electronics in the hole, then filling said hole with

epoxy - leaving a flat surface level with the surrounding consolidated aluminum. Following, aluminum tapes were welded across this flat surface using UAM.

Typically, rolled Galfenol is sectioned into sheets about 0.4 in (10.16 mm) wide. Narrower sections are manufacturable, however, sufficient active material must be present to yield easily measurable changes in flux density (for the case of an induction coil-based sensor). Thus, 0.4 in wide material was used. Challenges arise in embedding material of this breadth. For the mild UAM parameters used to embed sensitive parts into an Al matrix, metallic bonding is unlikely to occur between Al and steel (and therefore between Al and Galfenol). Therefore, when welding these materials, only 60 % of the total foil width is available to bond around the embedded elements. In this respect, the complexity of embedding in [27, 37, 50] is noticeably less, as a much higher percentage of the foil width could bond to the substrate. Research has proved possible the embedding of 0.4 in wide active materials [29], but without wound induction coils.

The embedding method used in [60] is not desirable for the manufacture of Al-Galfenol composite sensors. For the sensor to function, a coupling between bulk deformation and Galfenol deformation must be achieved. Without sufficient coupling, the mechanical response, and therefore the magnetic response, of the Galfenol would be minimized. Consequently, it is desirable to create the Al-Galfenol composite such that the consolidated Al sheet, which encapsulates the active material, makes an interface with said active material. This has been shown to produce mechanical interlocking at the interface, which improves the coupling between active material and substrate, even if metallic bonding does not occur [29].

For induction coil-based energy harvesters, the working principle is as follows: (1) the active material is wound with an induction coil and incorporated into a structure, (2) stresses developed in the active material cause changes in magnetization of said material, and (3) the magnetization changes produce a current in the wound coil and therefore power output.

2.1.1 Composite and Embedded Materials

Electrical steel sheets with dimensions of 3 in length, 0.4 in width, and 0.018 in thickness (76.2 mm x 10.16 mm x 0.4318 mm) were used as a substitute for Galfenol. This material was chosen due to its availability, low cost, and mechanical properties similar to those reported for Galfenol. One discrepancy between the materials is their elongation at break, where Galfenol is brittle (for compositions having higher magnetomechanical responses) [64] but the electrical steel used is quite ductile. Induction coils were wound using insulated, AWG 31 copper wire having an outside diameter of 0.01 in (0.254 mm). Base plates (0.1 in or 2.54 mm thick) and foils (0.006 in or 0.1524 mm thick) used for UAM welding were made of Al 3003-H18.

2.1.2 Build Preparation

Sheets of electrical steel were wound with one layer of Kapton insulation tape, adhesive side facing outward. The copper wire was wound around the steel, on top of the Kapton tape layer. Another layer of Kapton tape was applied on top of the wound wire and the lead wires. For each specimen, a groove with variable depth was machined into a base of Al 3003-H18 or into previously consolidated layers of Al 3003-H18 to house the specimens. Steel specimens were then bonded into the milled grooves using M-Bond strain gage adhesive. An example aluminum base plate with

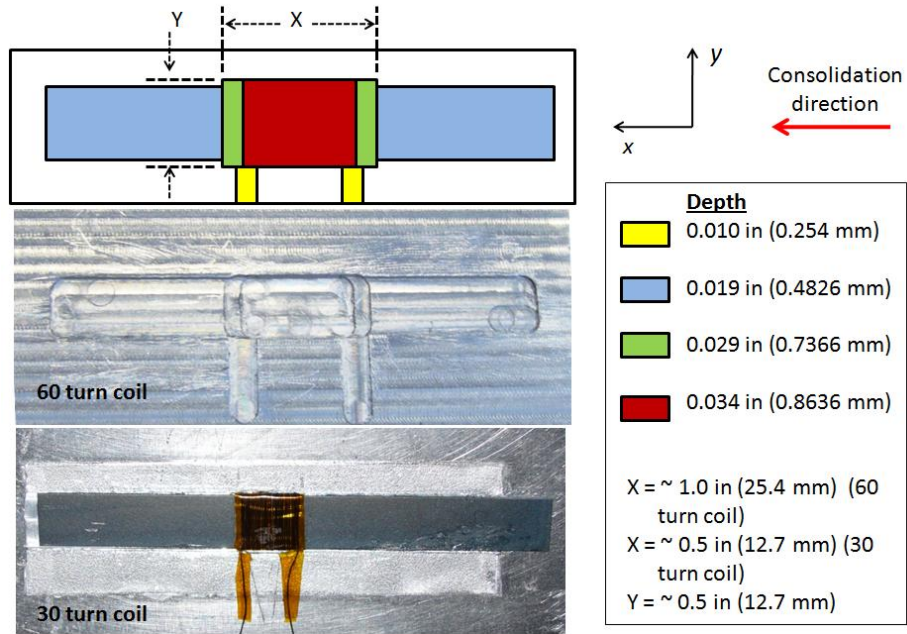


Figure 2.1: Induction coil build preparation

milled grooves, a schematic of the milled grooves, and an example build ready for embedding are shown in Figure 2.1.

The steel was roughly flush with the surrounding surface of the base aluminum, considering an adhesive thickness of about 0.025 mm. A total of nine builds were completed: six builds with 30 turn induction coils, and three builds with 60 turn induction coils.

2.1.3 UAM Process Parameters

The UAM system described in Section 1.2.4.1 was used for all welding trials. Table 2.1 reports the UAM process parameters used for each of the embedding trials. The parameters used were similar to those typical of embedding using Al 3003-H18

foils [29]. The number of tapes column refers to the number of non-consolidated Al 3003-H18 foils that were welded to the build surface during a single welding pass.

Table 2.1: Parameters for induction coil embeds

Build	Coil Number of Turns	Number of Tapes	Amplitude - μm	Normal Force - lbf (N)	Travel Speed - $\frac{\text{in}}{\text{s}}$ ($\frac{\text{mm}}{\text{s}}$)
1	30	2	31.2	1000 (4448.2)	1 (25.4)
2	30	2	31.2	1000 (4448.2)	1 (25.4)
3	60	2	31.2	1250 (5560.3)	1 (25.4)
4	60	2	31.2	1250 (5560.3)	1 (25.4)
5	30	3	31.2	1250 (5560.3)	1 (25.4)
6	30	3	31.2	1400 (6227.5)	1 (25.4)
7	60	2	36.4	1400 (6227.5)	1 (25.4)
8	30	2	31.2	1400 (6227.5)	1 (25.4)
9	60	2	31.2	1400 (6227.5)	1 (25.4)

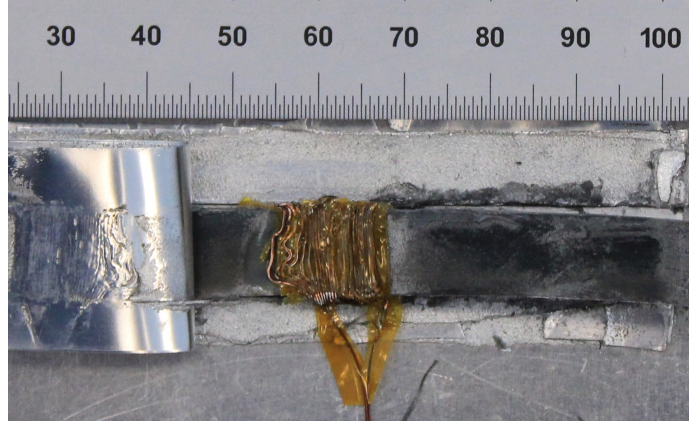


Figure 2.2: Insulation-stripped and deformed induction coil resulting from minimal Al bonding around coil (top Al foils manually peeled back for visualization of coil)

2.1.4 Results

For each trial, the wound induction coils did not have continuity at the leads (they were shorted to the Al tapes or base plate). Builds 1 through 4 resulted in sparse bonding of the Al tapes to the base and little plastic flow of said tapes around the coil components. It is theorized that this was a result of milling the grooves into Al tapes that were previously consolidated onto the base plate. The VHP UAM system used for consolidation does not have automatic tape feeding nor machining capabilities. Thus, it was difficult to consolidate the initial Al tapes onto the base plate in a neat and even stack. Further, grooves were milled on a separate machine and a facing pass before groove milling had not been completed. As a result, a height gradient from one end of the build to the other may have existed. Due to the minimal bonding of Al tape to Al base layers, the wound coils experienced a significant portion of the loading and therefore had insulation stripped off and were severely deformed in some cases, as shown in Figure 2.2.

Moving forward, specimens 5 through 9 were bonded into grooves milled directly in the base plate. This resulted in far less deformation of the induction coil exposed to the welding interface and greater consolidation of Al around the embedded elements. The coil of build 7 was severely deformed with much insulation removed, likely due to the high vibration amplitude used during embedding.

Also, it was noticed that a number of coil shorts were occurring where two strips of Kapton tape met¹⁸. In these locations, the normal force and vibrations separated the gap between strips of Kapton tape, which exposed the wires and melted their insulation. Therefore the induction coils for builds 8 and 9 were protected by applying Kapton tape along the x-direction (shown in Figure 2.1), which prevented tape seams from occurring. This resulted in almost no deformation of the wound coils as seen in Figure 2.3 and an inability to locate the short in the coil. Further, build 9 was fully embedded with welding occurring around the entirety of the steel sheet, wound coil, and even between the coil lead wires, as seen in Figure 2.4.

2.1.5 Analysis and Discussion

Complete embedding of a steel sample wound with a 60 turn induction coil was achieved by (1) milling a groove directly into a flat base plate of Al to house the sample, (2) applying a layer of Kapton insulation tape such that no tape seams occurred on the surface of the build, and (3) ultrasonically welding two non-consolidated Al foils over top with the parameters: 1400 lbf (6227.5 N) normal force, 31.2 μm amplitude, and 1 in/s (25.4 mm/s) travel speed. Despite the embedding success, the coil was shorted. To reduce the possibility of the coils shorting, it is hypothesized

¹⁸tapes were wound in the y-direction as shown in Figure 2.1 resulting in tape seams also in the y-direction

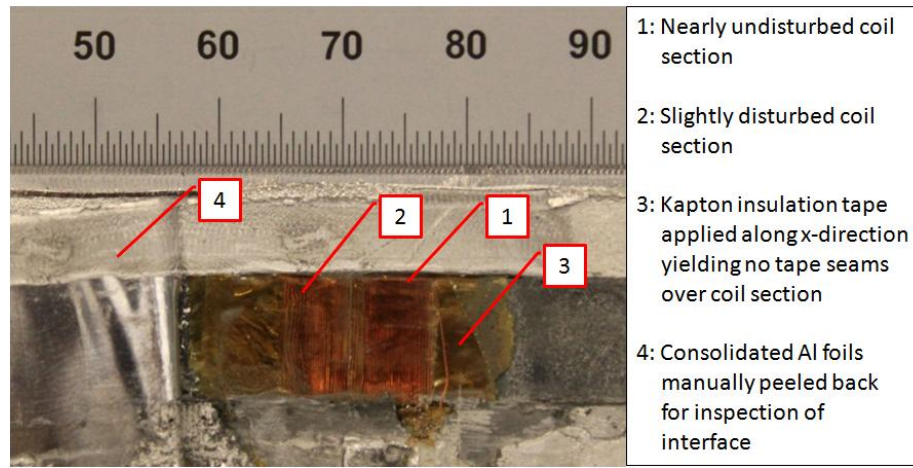


Figure 2.3: Weld interface of 30 turn induction coil build with no Kapton tape seams

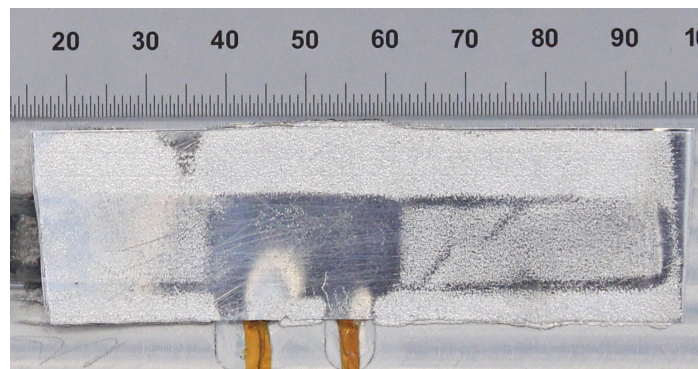


Figure 2.4: Fully embedded 0.4 in wide steel specimen with wound 60 turn induction coil

that the insulation on the wire should be increased or a stronger conductor or insulator material should be used. Of these two, the insulation thickness is thought to be most significant, because it was discovered that a coil could be embedded with very little or no deformation. However, the slight deformation or a relative motion between windings caused the insulation to be removed. Thus, increased thickness will further shield the wire from the elevated temperatures and shear forces that occur at the welding interface. The embedding of relatively large diameter wires has been accomplished with no damage to the wire in the case where the wire has a higher yield strength than the aluminum [37]. This resulted in significant flow of aluminum around the wires with no deformation of the embedded wires. Thus, coil survivability can be increased if a stronger conductor material or insulator material is used.

Other methods exist to measure the change in magnetization developed in the Galfenol as a result of changes in composite stress. One promising method is the use of giant magnetoresistance (GMR) sensors, which can detect minute changes in magnetic fields. GMR sensors are small chips that may prove ideal for embedding into active composites. One downside of this technology is that only sensing and not energy harvesting can be accomplished, because the sensors require input power to operate.

2.2 Iron-Gallium Embedding

A Galfenol-aluminum composite (using non-rolled Galfenol) has been previously produced using the UAM process in [29]. This was accomplished by (1) machining a groove (equal in depth to the thickness of Galfenol) into a flat plate of Al, (2) bonding of the Galfenol into the groove using strain gage adhesive, (3) filling in

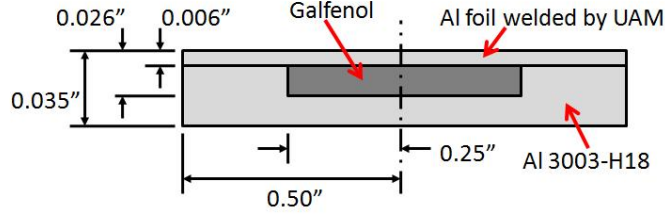


Figure 2.5: Cross-section of the desired Galfenol-aluminum active composites

remaining machining gaps with glazing putty, and (4) welding a single Al foil on top. To replicate the results of [29] and to test the embedding ability of newly available rolled Galfenol material, Al composites with non-rolled and rolled Galfenol active elements were investigated. As presented in Section 1.2.3.2, rolled Galfenol material is preferred over monolithic specimens for a variety of reasons. Thus, it is desirable to develop an active composite containing a recently developed rolled Galfenol material. Figure 2.5 shows a cross-section of the desired active composite.

2.2.1 Composite and Embedded Materials

For UAM welding, 0.006 in (0.1524 mm) thick Al 3003-H18 foils were used. Builds were prepared on Al 3003-H18 plates 0.1 in (2.54 mm) thick. The aforementioned Al plates were bolted to a low-carbon steel base plate 0.5 in (12.7 mm) thick, which was then clamped in four locations to the UAM machine. An example arrangement of consolidated Al foil, Al plate, and steel base plate used for UC is shown in Figure 2.6.

Highly textured Bridgman Galfenol steel sheets with nominal compositions of 18.4 at% Ga plus 1002 steel alloying additions were purchased from ETREMA Products, Inc. These sheets have dimensions of 0.015 in (0.381 mm) thickness, 0.4 in

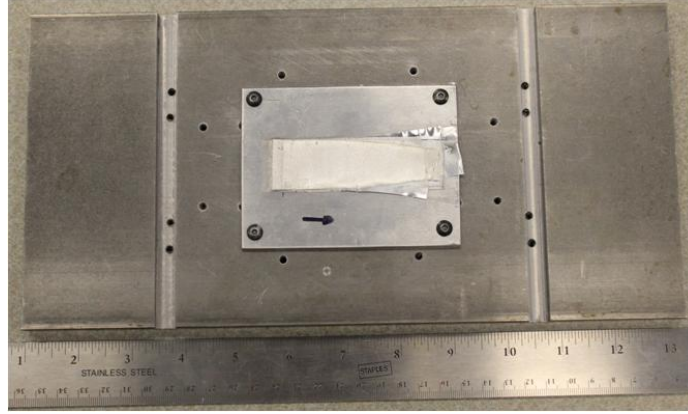


Figure 2.6: Fixture used to clamp welding plates to UAM machine: Al 3003-H18 plate bolted to steel base plate

(10.16 mm) width, and 4.0 in (101.6 mm) length, and were machined by wire EDM from highly textured rods. This material will be referred to as EDM cut Galfenol steel throughout this research.

Rolled sheets of Bridgman Galfenol steel with a high degree of texture and nominal compositions of 18.4 at% Ga plus low-carbon steel alloying additions were also purchased from ETREMA Products, Inc. These sheets have dimensions of 0.018 in (0.4572 mm) thickness, 0.5 in (12.7 mm) width, and 3.0 in (76.2 mm) length. This material will be referred to as rolled Galfenol steel throughout this research. These rolled sheets were produced by (1) melting 99.99 % purity Ga with low carbon steel, then chill casting into an ingot, (2) hot rolling, warm rolling, and cold rolling the ingot with an intermediate anneal, (3) heat treating under protective atmosphere to induce recrystallization and grain growth, (4) machining 0.5 in (12.7 mm) by 3.0 in (76.2 mm) samples from the rolled sheets by wire EDM [66].

2.2.2 UAM Process Parameters

The UAM system described in Section 1.2.4.1 was used for all welding trials. Unless specified otherwise, all embedding trials were performed using parameters of 1200 lbf (5337.9 N) normal force, 31.2 μm amplitude, and 1 in/s (25.4 mm/s) travel speed.

2.2.3 Composite Development

Three initial builds (builds 1, 2, and 3) were created by following the methods presented in [29], except that grooves were machined into stacks of 6 Al foils that had been previously welded onto an Al plate using UAM (in an effort to produce composites made entirely of Galfenol and ultrasonically consolidated aluminum). An additional alteration was a change in milling depth. For the single EDM cut Galfenol steel sample (build 3), a 0.02 in (0.508 mm) groove was milled to house the 0.015 in (0.381 mm) sample and allow for an adhesive layer as well. For similar reasons, a 0.025 in (0.635 mm) groove was milled to house the 0.018 in (0.4572 mm) rolled Galfenol steel sample. The thickness of the adhesive layer was overestimated, because the surface of the Galfenol samples were 0.002 – 0.004 in (50.8 – 101.6 μm) below the Al surface. In each of these trials, the Galfenol samples fractured and were ejected or partially ejected from the milled groove, and shearing of the welded Al foil occurred along the edges of the milled groove. Before and after pictures of an example build is shown in Figure 2.7. Surprisingly, the consolidated Al foil had a large amount of texturing directly above the Galfenol. This indicates that slip between the sonotrode and Al foil did not occur at this location, and suggests that flow of the foil occurred likely causing good mechanical coupling between foil and Galfenol.

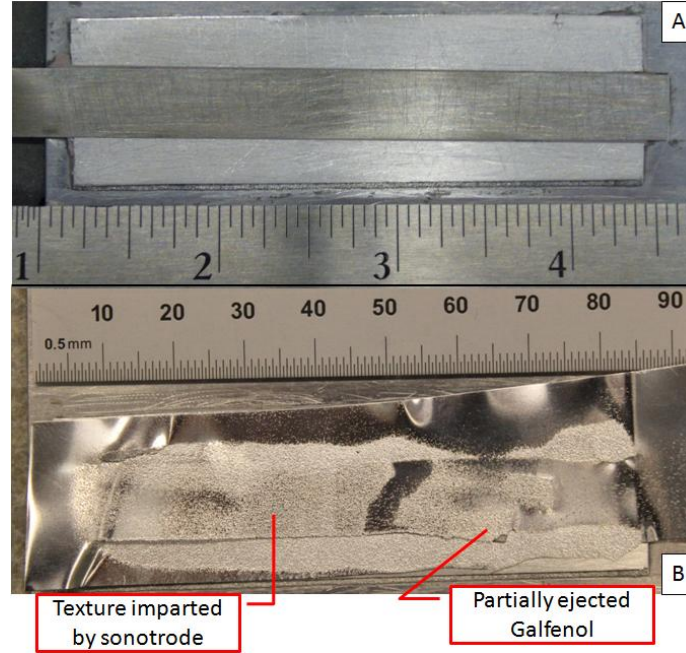


Figure 2.7: EDM cut Galfenol steel build 3 (A) before and (B) after

The main culprit for the unsuccessful builds above was likely an unfavorable contact pressure distribution, which caused the Al foil to strain excessively over the Al shoulder that ran alongside the Galfenol, due to its recessed location. Further, it has been shown that there exists a maximum height to width ratio (H/W) for ultrasonic consolidation [59]. Due to the milled groove throughout the length of the Galfenol builds, two narrow ribs ($H/W \approx 0.1$) are formed on either side of the Galfenol that run the length of the builds. In [59], the maximum H/W was determined to be roughly 1, calculated from builds welded with half the amplitude used in this research. The maximum H/W as a function of amplitude is not known, but it is reasonable to assume that it will decrease as vibration amplitude increases. Therefore, I theorize that excessive deflection of the ribs that sandwich the Galfenol, caused by the large

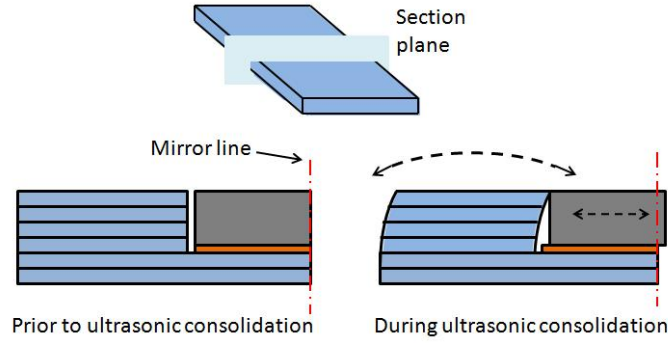


Figure 2.8: Cross sectional view of rib deflection during the UAM process

vibration amplitude, may have caused the adhesive to shear, which resulted in failure of the embed. A depiction of this is shown in a cross-sectional view of the composite in Figure 2.8, where the mirror line is a line of symmetry in the cross-section. During UAM welding, the aluminum ribs surrounding the Galfenol vibrate in phase with the welding horn, or sonotrode. This imparts a horizontal force on the Galfenol. Since the shear strength of adhesives is low, this force is sufficient to shear the adhesive layer, leading to fracture of the Galfenol as it moves from the bonded location.

To combat the issues discussed above, changes were made to the build preparation. The depth of the grooves was decreased, and sanding using 50 grit paper was completed such that a completely flat, even surface was achieved. Also, the grooves were machined directly into the Al plates described in Section 2.2.1, to improve the stiffness of the Al surrounding the Galfenol. Further, qualitative contact pressure distributions were obtained using pressure sensitive film (Pressurex “high” pressure film manufactured by Sensor Products, Inc.). Accuracies for the contact pressures are estimated at $\pm 15\%$ by the manufacturer. Contact pressure measurements were taken in ambient with approximately $22\text{ }^{\circ}\text{C}$ and 50 \%RH . This film was placed between the

sonotrode and a non-consolidated Al foil (that had been placed on top of the build in the orientation used for UAM welding). To obtain the contact pressure distributions, the following process parameters were used: 400 lbf (1779.3 N) normal force, 0 μ m amplitude (ultrasonics off), and 1 in/s (25.4 mm/s) travel speed.

Two additional builds (builds 4 and 5) were prepared using the preparation changes listed above and the rolled Galfenol steel specimens. In each case embedding of the Galfenol failed, but the Galfenol sample did not experience fracture nor noticeable deformation. Post welding pictures and pressure films, including an example prewelding picture are shown in Figures 2.9 and 2.10. Following ultrasonic consolidation, the Galfenol samples in builds 4 and 5 each had 2 Al nuggets on their surface. Micrographs of the interface between these nuggets and the Galfenol have not been obtained. Therefore, whether the nugget was welded to the Galfenol or just significantly interlocked could not be assessed, although mechanical interlocking without welding is expected due to the large asperity height caused by the coarse sandpaper. The nuggets can likely be attributed to the rigorous sample preparation, which involved sanding with 150 grit sandpaper and degreasing with isopropyl alcohol. Sanding removes any oxide layer on the surface of the Galfenol and creates relatively large crevices between asperities for the Al foil to flow into.

In build 4, the Al foil sheared along the front edge of the Galfenol. The cause was the sonotrode starting location during the welding pass. When the sonotrode is contacting the build prior to the edge of the Galfenol, the area supporting the sonotrode normal force was reduced, due to the very soft body filler. This resulted in increased compression. When the sonotrode passes over the Galfenol section of the build, the load-bearing area increases leading to decreased compression of the

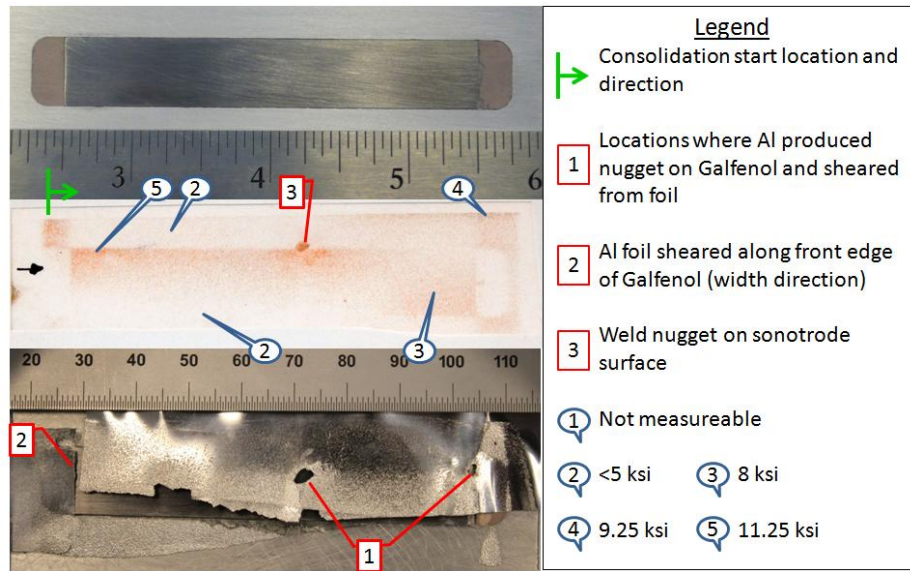


Figure 2.9: Before and after welding, and pressure film of rolled Galfenol steel UAM build 4

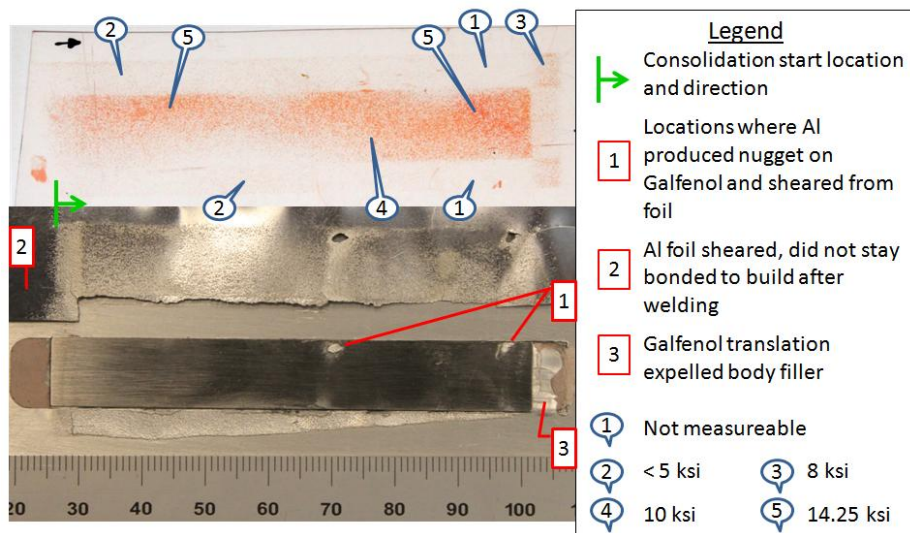


Figure 2.10: Post welding and pressure film of rolled Galfenol steel UAM build 5

build. Therefore, as the sonotrode reached the edge of the Galfenol, it experienced a step input in build height. This led to excessive strain in the Al foil and its subsequent shearing. Consequently, the welding process for build 5 was altered so that the sonotrode started near the edge of the Galfenol (where Galfenol shared the load with the surrounding Al), as shown in Figure 2.10.

While the surface of build 5 was sanded flat using sandpaper fitted around a large flat metal block, the pressure-sensitive film has the appearance of a build in which the Galfenol is located slightly above the Al surface. A more likely explanation for the contact pressure distribution is that Galfenol is much stiffer than the aluminum 3003-H18. The elastic modulus of Galfenol is typically published as in Table 1.2, but this is only valid in the $\langle 100 \rangle$ crystal direction. The specification of the $\langle 100 \rangle$ direction is usually dropped, because the elastic modulus of interest is typically the modulus along the actuation axis, or $\langle 100 \rangle$ direction. The direction of the normal force applied during the UAM process is in the crystallographic $\langle 110 \rangle$ direction. In the $\langle 110 \rangle$ direction, Galfenol has an elastic modulus of ~ 160 GPa [36], which is ~ 2.5 times that of the surrounding Al 3003-H18. Thus, for flat build surfaces, the Galfenol will always sustain the majority of the normal loading. Without ample pressure between aluminum surfaces, solid-state welding cannot be achieved.

The cause of failure for build 5 is likely asymmetry in bonding along the welding direction. Due to the near zero contact pressure on the aluminum sections, the sonotrode slipped across one side of the Al foil (leading to zero welding on that side), but stuck to the opposite side of the Al foil (leading to welding of Al foil to Al substrate). Thus, the Al foil experienced alternating cycles of tension and compression

along the width of the foil as half of the foil moved with the sonotrode vibration and the other half was not perturbed. This lead to shearing of the Al foil.

2.2.4 Analysis and Discussion

Reasons why embedding success was achieved in [29], and not in this research is difficult to reconcile, due to the ignorance of contact pressure distribution in [29], which was shown to play a critical role in this research. The key difference between the studies is the width of Galfenol samples embedded (0.4 in for the successful embed vs. 0.5 in for the unsuccessful embeds). The reduction in the available welding surface (from 0.6 in to 0.5 in) is significant, and increases the difficulty in producing a successful solid-state weld using UAM. It is therefore theorized that a critical width may exist, above which embedding is either impossible or very difficult.

From the embedding trails carried out, much insight into the ideal embedding method has been gained. Moving forward, a few key ideas are clear. First, if Galfenol is level with the surrounding aluminum, the Galfenol bears the majority of the load, leading to great difficulty in producing a solid-state weld between aluminum foil and aluminum base plate. Second, the contact pressure distribution plays a critical role in the embedding process, where pressure concentrations likely lead to fracture of the Galfenol. Third, build preparation that includes sanding the Galfenol surface with 150 grit sandpaper and then degreasing leads to significant mechanical interlocking or welding between the Al foil and Galfenol, for the UAM parameters used. Therefore, future attempts to embed the rolled Galfenol steel samples will follow the same sample preparation procedure, but with Galfenol very slightly recessed below the surface of the aluminum in order to yield a more favorable contact pressure distribution.

CHAPTER 3

MAGNETIC TRANSDUCTION CIRCUIT

3.1 Design

This section details the constraints and design of critical components of the magnetic transduction circuit. Two configurations of the magnetic circuit are desired: a material characterization configuration and a cantilever beam vibration configuration. For the material characterization setup, the magnetic circuit will provide control of the magnetic domain, while the composites are loaded in tension and compression using a load frame. For the cantilever beam vibration configuration, the magnetic circuit will provide control of the magnetic domain and a rigid clamping of the composite as a cantilever, while interfacing with a shaker table or pushrod-type electromagnetic shaker.

3.1.1 Magnetic Flux-Linking Elements

Important properties for the magnetic circuit elements used to flux link the drive coils to the composite are the magnetic permeability, electrical resistivity, and the saturation magnetization or flux density. For this reason, Metglas cores were initially the material of choice, with their saturation flux density around 1.5 T, very high

permeability, and high resistivity [48]. Additionally, the cores are formed by laminating Metglas ribbons about $25\text{ }\mu\text{m}$ thick. However, the Metglas cores are difficult to manufacture and require specialized tooling, which limits custom designs. Machining of production Metglas cores also proved very difficult due to the material's very high hardness. Machining by wire EDM was unsuccessful due to the discontinuity in metallic elements through the thickness of the cores (resulting from the laminating adhesive). For the reasons stated, electrical steel laminations, which are a standard choice for DC motors and transformers, were selected instead of the Metglas cores. Electrical steel can have saturation flux densities around 2 T, mild resistivity, and high permeability [1].

Initial designs consisted of nearly U-shaped stacks of steel laminates, where the Al-Galfenol composites would complete the flux path and form an O-shape, and the drive coil would sit opposite the composite. This design, while simple, does not synthesize well with mechanical excitation from a shaker, due to its asymmetry. Further, the length of the single coil is constrained by the length of the composites, which need to be gripped at the ends during the material characterization setup. Thus, the design in Figure 3.1 was adopted. This design allows for two drive coils to be utilized, effectively doubling the magnetizing force through the composite in ideal situations. Slots in the stacks of laminates also allow the UAM composites to slide freely through the stacks, for use with a load frame, and complete the magnetic flux path concurrently. Further, the symmetric nature of the flux path should produce a very uniform flux path along the length of the composite in ideal situations.

During compressive loading of the composite, buckling becomes a concern. To prevent this, the distance between the protrusions, L , labeled in Figure 3.1 was limited.

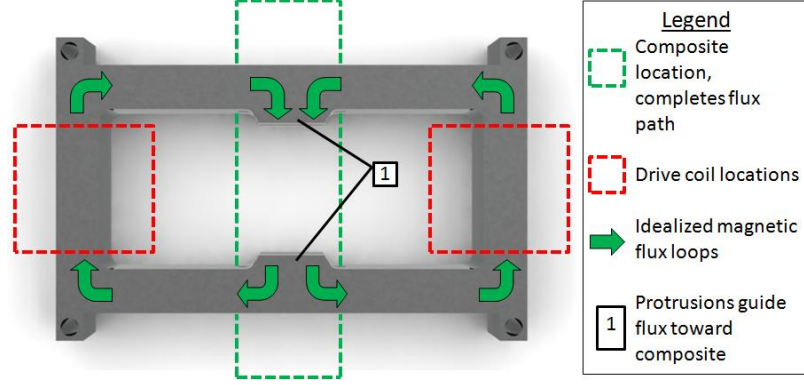


Figure 3.1: Design of electrical steel laminates used to flux link composite to drive coils

To increase the critical buckling load, L should be decreased. However, L is the region of the composite in which measurements will be obtained and is also linearly related to the length of the cantilevered composite beam. In order to have ample space for measurements and a beam that will easily deflect, L should be increased. To balance these opposing desires, a length, L , of 1 in (25.4 mm) was chosen. For this length, the critical buckling loads for both the composite (cross-section shown in Figure 2.5) and the Galfenol sheets (0.02 x 0.5 in or 0.508 x 12.7 mm cross-section) are summarized in Table 3.1. In this table, the pinned-pinned and fixed-fixed columns refer to the critical values calculated assuming the slots provide a pinned-pinned or fixed-fixed boundary condition, respectively, on the composite or Galfenol sheet. These values were calculated using Equation (3.1),

$$P_{cr} = \frac{\pi^2 EI}{L_e^2}, \quad (3.1)$$

where L_e is equal to L for pinned-pinned boundary conditions and $0.5L$ for fixed-fixed boundary conditions [11].

Table 3.1: Critical buckling loads and maximum compressive stress that can be developed in Galfenol for testing of Galfenol sheets and Galfenol-Al composites

	Galfenol sheet		Composite	
	Pinned-pinned	fixed-fixed	Pinned-pinned	fixed-fixed
Critical buckling load (N)	135.8	543.3	1535	6142
Maximum compressive stress produced in Galfenol (MPa)	21.05	84.22	64.49	257.9

The critical buckling loads in Table 3.1 were calculated directly from Equation (3.1). The compressive stress developed in the Galfenol that corresponds to each critical buckling load was calculated by considering the aluminum and Galfenol of the composite as two springs in parallel. The values in Table 3.1 are estimations that do not include magnetic field-dependent elastic properties, potential slip between aluminum and Galfenol surfaces, nor other effects due to the magnetic and mechanical coupling. For calculations, an elastic modulus of 64 GPa was used for Galfenol in the $\langle 100 \rangle$ direction [76].

3.1.2 Drive Coils

To determine the drive coil, or drive solenoid, number of turns and length, rolled Galfenol material constraints and geometry constraints were considered. As presented in [29], a magnetizing field of about 25 kA/m is required to saturate the 0.015 in (381 μm) thick Bridgman Galfenol steel. Also, as shown in Figure 1.4, as the applied compressive stress along the length of Galfenol increases, the magnetizing field required for saturation increases. This is seen as a widening of the “butterfly” curve in

the strain vs. magnetic field plot. Thus, to be conservative, a maximum magnetizing field of 60 kA/m along the composite is desired.

Due to air gaps and imperfections throughout the magnetic circuit, the amount of magnetic flux generated along the composite will always be less than that generated at the center of the solenoids. A conservative safety factor of 1.5 was used to account for this, resulting in a maximum generated magnetic field of 90 kA/m. In a perfectly symmetric magnetic circuit as designed in Figure 3.1, the magnetizing force generated by each coil sums to yield the magnetizing force through the composite. Consequently, each coil was designed to have a magnetic field strength of 45 kA/m.

Using Equation (1.3), the magnetic field strength at the center of each solenoid can be calculated as a function of the number of turns, current, and geometry. From the magnetic circuit design shown in Figure 3.1 and expanded upon in the following sections, geometry constraints for the coil inner radius, coil length, and coil outer radius were determined. Additionally, as a precaution, the coil current is limited to 1 A. From Equation (1.3), it was calculated that a coil thickness of ~ 0.6 in (15.24 mm) would yield the desired coil strength. However, the calculation assumed perfect winding of the coil. Therefore, a coil thickness of 0.75 in (19.05 mm) was chosen, which corresponds to ~ 3100 turns if perfectly wound.

3.1.3 Material/Composite Characterization Setup

To characterize the rolled Galfenol materials or the FeGa-Al composites (by obtaining the 4 sensing and actuation curves similar to Figure 1.4), a load frame must be used to provide bias mechanical stress during sensing and mechanical strain during actuation. In the characterization configuration, the magnetic circuit must allow the

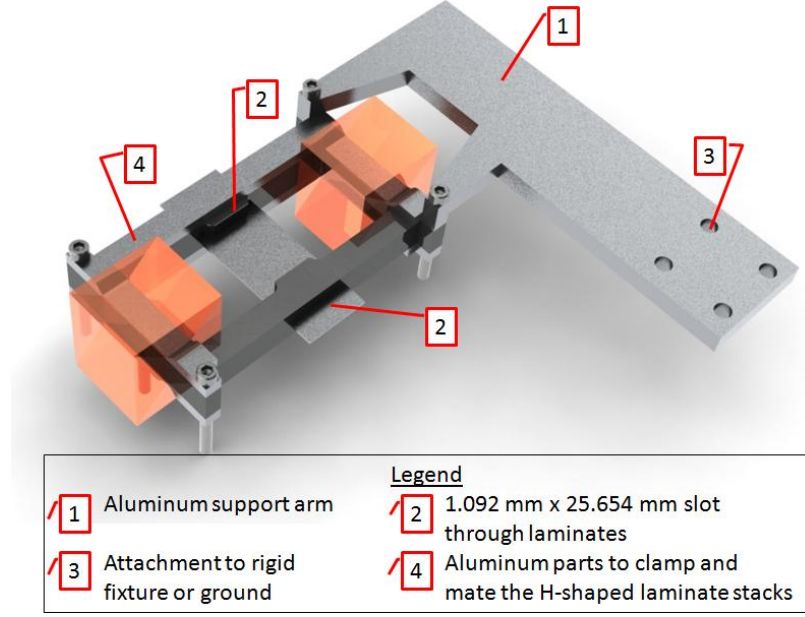


Figure 3.2: Design of magnetic circuit for use with a load frame during characterization testing

composite to strain freely, while maintaining a fixed position in space through rigid fixturing. To accomplish this, the setup shown in Figure 3.2 was designed.

The aluminum support arm shown in Figure 3.2 supports the weight of the magnetic circuit, while also magnetically insulating the magnetic system by isolating it from neighboring ferromagnetic materials. The slot through the electrical steel laminates allows the UAM composites to complete the magnetic flux path, while minimizing the adverse air gap between the composite and steel stack to 0.005 in (0.127 mm). The completed material/composite characterization setup of the magnetic circuit is shown in Figure 3.3.

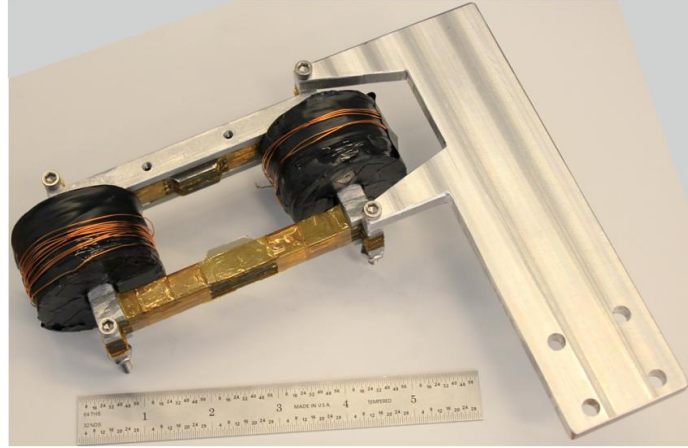


Figure 3.3: Material/composite characterization setup

3.1.4 Cantilever Beam Vibration Setup

In the cantilever beam vibration setup, the magnetic circuit will be used with a shaker table or electromagnetic shaker to induce beam bending. Sensor or energy harvester responses to mechanical excitations will be obtained with this magnetic circuit assembly. The aluminum support arm from the characterization setup is no longer needed, as the magnetic circuit will be supported by fishing line if used with the shaker (creating a pendulum of the circuit), or by the shaker table itself. The configuration shown in Figure 3.4 was designed to vibrate the magnetic circuit using the shaker table or shaker, while clamping the composite as a simple cantilever. The presence of the steel laminate stacks and drive coils in this setup will allow for precise control of the magnetic bias field applied to the composite. With the determination of the ideal magnetic field bias, the steel and drive coils can be replaced by permanent magnets, creating a small sensor package that can be realized for future Galfenol-based sensor applications. The design of this setup is identical to the characterization

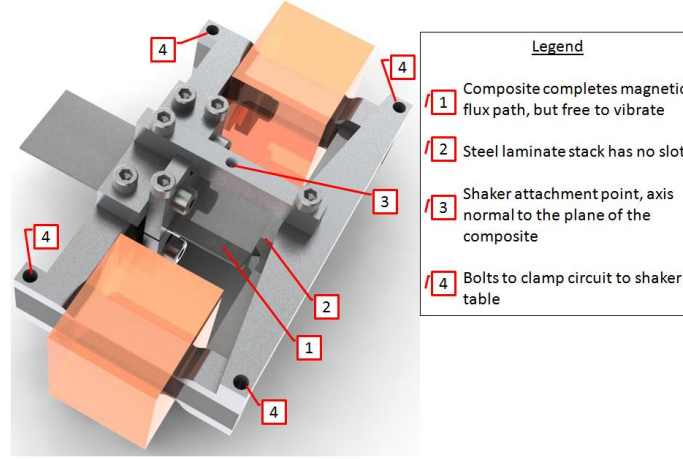


Figure 3.4: Design of cantilever beam vibration setup

setup, except for the aluminum support arm and the aluminum fixturing shown as an exploded view in Figure 3.5.

For the vibration configuration of the magnetic circuit, an electrical steel laminate stack with a slot is mated to and clamped to a stack without a slot. This allows the composite to complete the magnetic flux path and to vibrate freely, while minimizing magnetic flux losses by removing the superfluous slot near the cantilever beam tip. The shaker attachment point is oriented such that the shaker pushrod will be normal to the surface of the composite. It is also located midway between drive coils and midway between each electrical steel laminate stack. The as-machined cantilever beam vibration setup is shown in Figure 3.6.

3.2 Manufacture of Components

This section details specific manufacturing methods used for critical components of the magnetic transduction circuit.

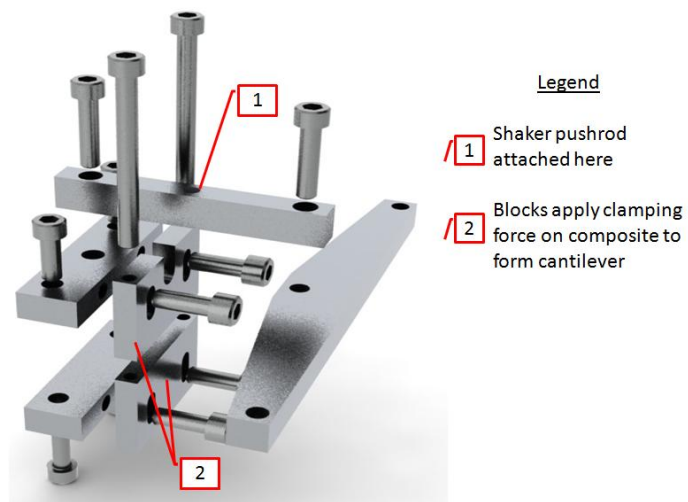


Figure 3.5: Exploded view of aluminum fixturing used to cantilever composite to magnetic circuit and interface with a shaker

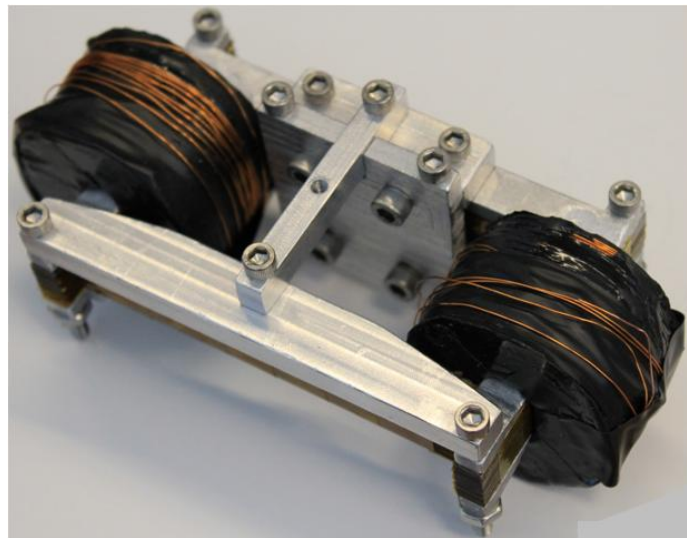


Figure 3.6: Cantilever beam vibration setup



Figure 3.7: Electrical steel laminate stacks; A and B used for material/composite characterization setup, A and C used for cantilever beam vibration setup

3.2.1 Electrical Steel Laminates

The electrical steel laminate sheets were machined by wire EDM for uniformity and accuracy. The purpose of using laminates instead of a bulk piece of steel is to reduce the eddy current losses that become significant during frequency operation of the magnetic circuit. To insulate the laminates from each other, 0.001 in (0.0254 mm) thick Kapton insulation film was cut to the shape of each laminate and applied between each layer. Following, the laminates were stacked, aligned, and secured with Kapton tape wound around the outside. Figure 3.7 shows the resulting laminate stacks.

3.2.2 Drive Coils

To produce a solenoid that would fit around the steel laminates, while also minimizing the air gap between the two, coils were wound onto an accurately milled block, which is shown in Figure 3.8. 26 AWG copper wire was chosen from the available wire as this was calculated to yield coils with the greatest magnetic field strength¹⁹.

¹⁹calculated using each coil's dimensions and maximum rated current

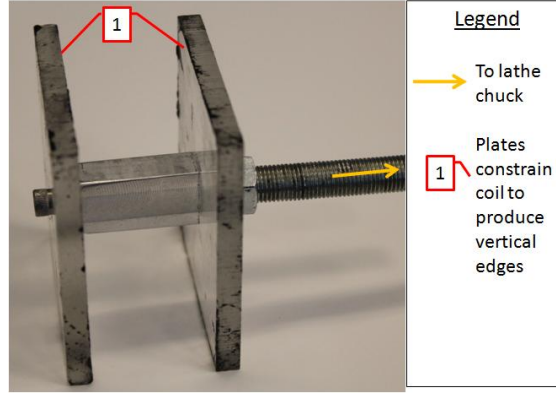


Figure 3.8: Machined block and fixture used to wind drive solenoids

To expedite winding and produce uniformly wound solenoids, coils were wound on a lathe. The thread cutting feature of the lathe was used to feed the wire along the coil length as the block rotated such that the gaps between windings were uniform and minimized. During coil winding, epoxy was applied every 2 layers. The resulting coils are shown in Figure 3.9.

Following production, the magnetic field strength of each coil in air was obtained by applying a 0.1 Hz sinusoidal current of 1.2 A to each. Magnetic field strength was measured using a Walker Scientific MG-4D gaussmeter and a HP245S axial Hall probe positioned at the center of the solenoid, parallel to the coil axis. The absolute value of field strength at coil current of -1 and 1 A was averaged over 12 cycles of applied current. The resulting averaged field strengths are given in Figure 3.9. Using the actual thicknesses of the coils and their corresponding maximum number of windings, a theoretical field strength could be calculated for each solenoid, using Equation (1.3). A winding efficiency, expressed as Equation (3.2), could also be calculated as,

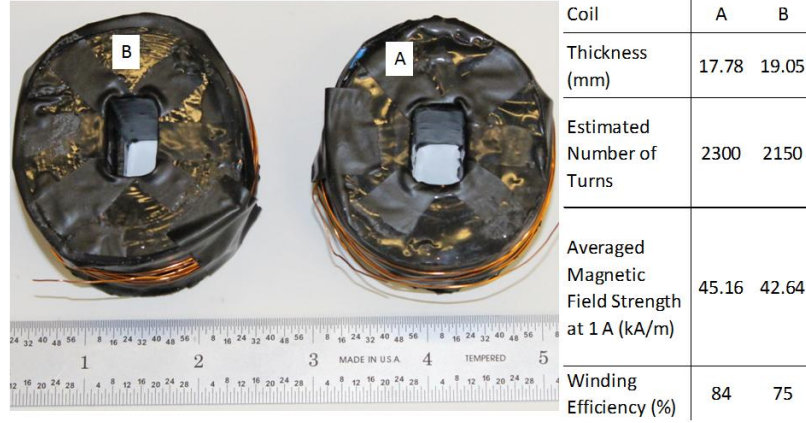


Figure 3.9: Drive solenoids and relevant dimensions and properties

$$\eta_{winding} = \frac{H_{actual}}{H_{theoretical}} = \frac{H_{actual}}{\frac{N_{max}i}{a_{1,actual}} \frac{F(\alpha_{actual}, \beta_{actual})}{2\beta_{actual}(\alpha_{actual}-1)}}. \quad (3.2)$$

The winding efficiency will be used in Section 3.3 for modeling of the solenoids.

3.3 Verification and Modeling

This section details the FEM model used to verify the magnetic design of the magnetic transduction circuit. Actuation of the UAM composites was also modeled. The modeling program used was COMSOL multiphysics with Matlab.

3.3.1 Galfenol Material Model

To model the behavior of Galfenol, the constitutive model developed by Evans was used [22]. This model was formulated into a finite element model for use with COMSOL and Matlab by Chakrabarti [5]. This model uses a piecewise-linear solution process that first utilizes COMSOL to calculate the first increment in magnetic flux density, $\Delta \mathbf{B}$, and mechanical strain, $\Delta \mathbf{S}$, at each node in the Galfenol domain.

Next, the spatially-dependent piezomagnetic coefficients are calculated from the initial stress and magnetic field at each node. Following, the incremental magnetic field and stress, $\Delta\mathbf{H}$ and $\Delta\mathbf{T}$ respectively, are calculated using the linear magnetostrictive constitutive law, Equations (1.15) and (1.16). After, the next increment in magnetic flux density and strain are calculated, and the process repeats. The characteristic curves of Galfenol are therefore traversed through linear approximations between steps. The accuracy of the model is thus dependent upon the step size of increments, due to increasing drift error as the step size is increased.

3.3.2 Magnetic Circuit Design Verification

3.3.2.1 Model Parameters and Development

To determine the magnetic flux path and magnetic field strength throughout the circuit, a 1:1 scale three-dimensional model of the composite characterization setup was created. The characterization setup was modeled instead of the vibration setup, because it was determined to be more critical with respect to flux losses. The characterization setup utilizes steel laminate stacks, each with a slot that creates an air gap around the composite. The vibration setup has only one laminate stack with a slot. While an air gap between the cantilevered beam tip and adjacent laminate stack exists (allowing the composite to vibrate freely between the stacks), its breadth can be controlled and its effect on the flux path is less severe.

Since aluminum is a paramagnetic material, its magnetic response to magnetic fields can be neglected. Therefore, the aluminum support arm, aluminum parts to clamp the laminates, and all bolts were replaced by air in the model. Further simplifications were applied by removing all fillets and replacing circular holes by square holes. Additionally, the solenoids were modeled as rectangular prisms, divided into

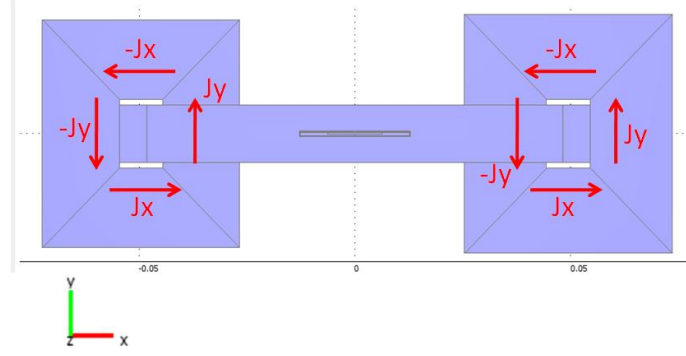


Figure 3.10: Simplified drive coils with current direction shown

quarters, with each segment carrying a current density in a single direction, as seen in a side view of the model in Figure 3.10. For the specified current densities the right-hand rule can be used, such that the magnetic fields produced from each coil would point out of the page.

Despite the simplifications, a number of important complexities were retained for accuracy. These complexities of the model are shown in Figure 3.11. The most important of these is a 0.005 in (0.127 mm) air gap between the composite and each of the steel laminate stacks. These complexities may significantly alter the magnetic flux path and result in nonuniform or incomplete actuation of the Galfenol.

Ideally, the two solenoids are identical, yielding the ideal magnetic flux path shown in Figure 3.1. However, a 5.74 % difference (calculated from Figure 3.9) exists between the magnetic field strength of the actual solenoids. This was incorporated into the COMSOL simulation by defining a specific current density (defined from the experimentally determined magnetic field strengths) and size for each coil. The constants used to define each coil are given in Table 3.2.

The maximum current density, J_{max} , was calculated from Equation (3.3),

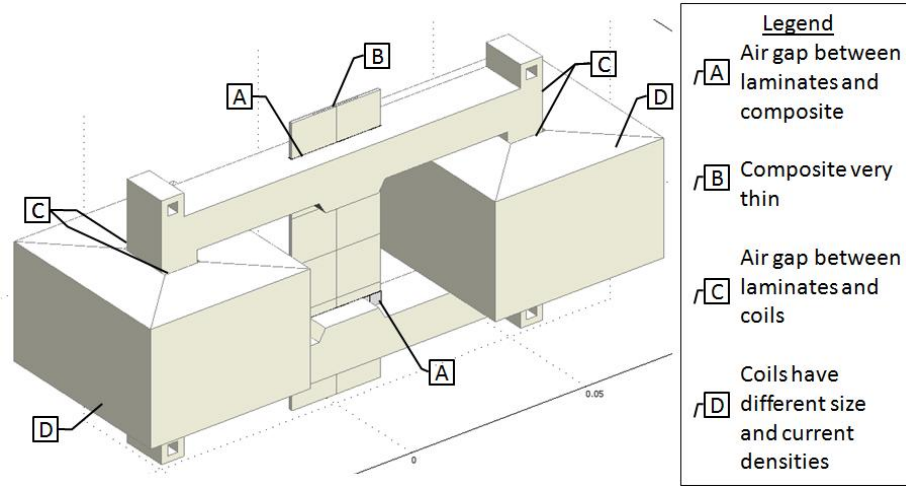


Figure 3.11: Complexities of the magnetic transduction circuit retained for finite element modeling

Table 3.2: Solenoid constants used for finite element simulations

	Units	Coil A	Coil B
Conductivity	$\frac{S}{m}$	5.88E+07	5.88E+07
C/S area of wire, AW	m^2	1.28E-07	1.28E-07
Resistance, R	Ohm	35.1	37.9
Max voltage, V_{max}	V	7.02	7.58
Max current	A	0.2	0.2
Winding efficiency, $\eta_{winding}$	no units	0.838	0.751
Wire packing factor, $\eta_{packing}$	no units	0.8162	0.8162
Max current density, J_{max}	$\frac{A}{m^2}$	1.07E+06	9.58E+05

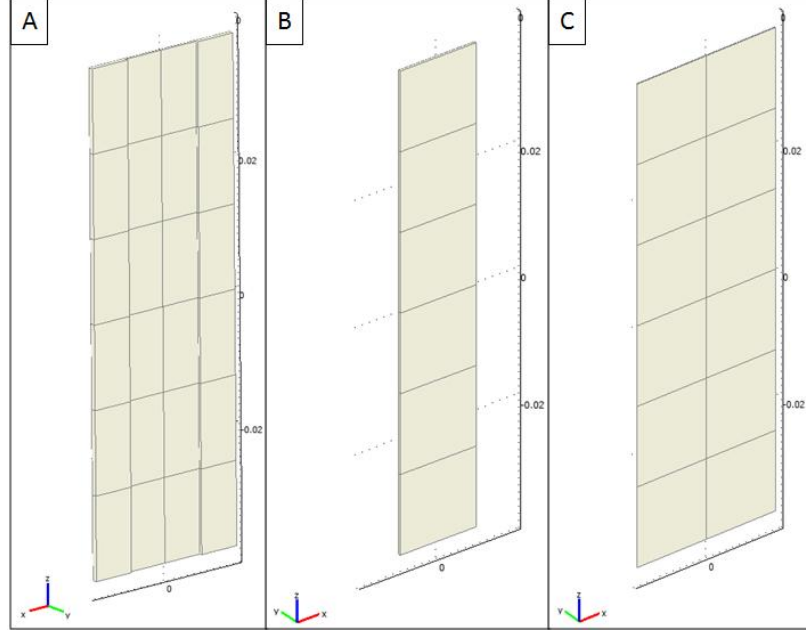


Figure 3.12: Discretization of composite domains: (A) aluminum substrate, (B) Galfenol, (C) UAM aluminum foil

$$J_{max} = \frac{V_{max} \cdot \eta_{winding} \cdot \eta_{packing}}{R \cdot AW}. \quad (3.3)$$

In Table 3.2, the wire packing factor is a correction factor accounting for the efficiency of packing circular wires into a rectangular space. It was calculated by considering a 2D rectangular space and maximizing the number and spacing of circles within that space.

Due to the large difference in size between the composite thickness and the surrounding geometry, the meshing algorithm fails, as it attempts to create a mesh with very large gradients in element size. To overcome this, the composite geometry was split into many domains, as shown in Figure 3.12. A similar procedure was used for the air gap between the composite and the electrical steel laminates.

The mechanical and magnetic constants used to define the steel and aluminum domains are displayed in Table 3.3. The actuation frequency for the simulations was 1 Hz.

Table 3.3: Mechanical and magnetic constants of electrical steel and Al 3003-H18 used for finite element simulations

	Units	Electrical steel	Al 3003-H18
Magnetic permeability	$\frac{\text{N}}{\text{A}^2}$	$10e3\mu_0$	μ_0
Elastic modulus	Pa	2.00E+11	6.89E+10
Poisson's ratio	no units	0.3	0.33
Damping coefficient	$\frac{\text{N}}{\text{m/s}}$	100	100
Density	$\frac{\text{kg}}{\text{m}^3}$	7860	2730
Conductivity	$\frac{\text{S}}{\text{m}}$	2.06E+07	2.31E+07

3.3.2.2 Results and Discussion

The COMSOL model was solved for the mesh shown in Figure 3.13 (domain representing air not shown), having 64,397 elements and 353,922 degrees of freedom. The mechanical boundary condition is also shown in Figure 3.13. The magnetic boundary condition was a flux density of zero on the outer surface of the large air volume surrounding the circuit (seen as a wireframe in Figure 3.15). To test convergence, the model was solved four times. With each run, the magnitude increase in current to the coils for each increment of the solution process was decreased. Convergence of the flux density along the Z-direction, or length direction, of Galfenol is shown in Table 3.4. The flux density values shown in the table are averaged over the Galfenol domains located between the steel laminates. The percent difference between a run and the previous run is calculated in the table, showing the convergence. The magnitude of

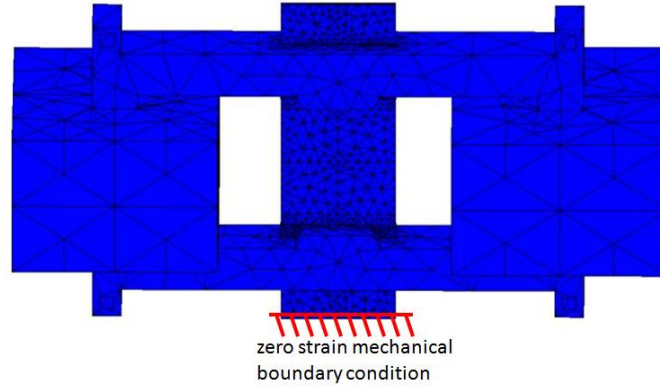


Figure 3.13: Mesh used to solve COMSOL simulations

the flux density near saturation and above saturation is artificially high due to the step size of coil current. For increased accuracy, the step size can be decreased, and the saturation flux density will approach the experimental value of about 1.5 T [45]. However, for the purpose of this simulation, this drift error is acceptable, and will have little effect on the overall magnetic flux path. This is known, because the magnetic flux path of simulations 2 and 3 were not significantly different from simulation 4.

Table 3.4: Convergence of flux density in Galfenol

Run	Number of elements	Degrees of freedom	Incremental current (A)	Flux density in Z-direction, BZ (T)	Percent difference in BZ (%)
1	64,397	353,922	0.141	3.30	-
2	64,397	353,922	0.033	2.00	49.1
3	64,397	353,922	0.013	1.75	13.3
4	64,397	353,922	0.008	1.67	4.7

To verify the magnetic transduction circuit design, the path of the magnetic flux loops throughout the circuit and the distribution of flux throughout the Galfenol were obtained from simulation 4. Figure 3.14 shows the progression of the magnetic flux path as the current to the coils is increased. The red loops are streamlines of the magnetic flux density with components: B_X , B_Y , B_Z . Each plot has 20 streamlines. Saturation of the Galfenol was reached at a current of 0.112 A to each coil (at a magnetic field of about 5 kA/m over the Galfenol spanning between the sides of the steel laminates). Therefore, at currents above 0.112 A, the Galfenol is in the forced magnetostriction region, which occurs after the Galfenol is fully magnetized in the direction of the applied field. As seen in Figure 3.14, the flux is concentrated in the Galfenol and the majority of flux loops follow the idealized magnetic flux path shown in Figure 3.1. An interesting result of the simulation, is that very little or none of the flux generated by the smaller solenoid follows the idealized path and aids in saturating the Galfenol. This is solely due to the difference in strength of each coil, and was an expected result, because the experimental strengths were known. This difference can be accounted for by feedback control of the coil currents. Despite, the simulation shows that the magnetic flux “lost” from the circuit (meaning not contributing to the magnetization of the Galfenol) was minimal.

The distribution of flux throughout the Galfenol should be uniform throughout the region where measurements will be obtained. Due to the coupling of the magnetic and mechanical domains, if nonuniform flux exists in the Galfenol, there will be gradients in Galfenol magnetostriction and magnetization. This will yield internal stresses at domain boundaries and adverse magnetic interactions between domains of different orientation. The result of this will be an increased difficulty in saturating Galfenol and

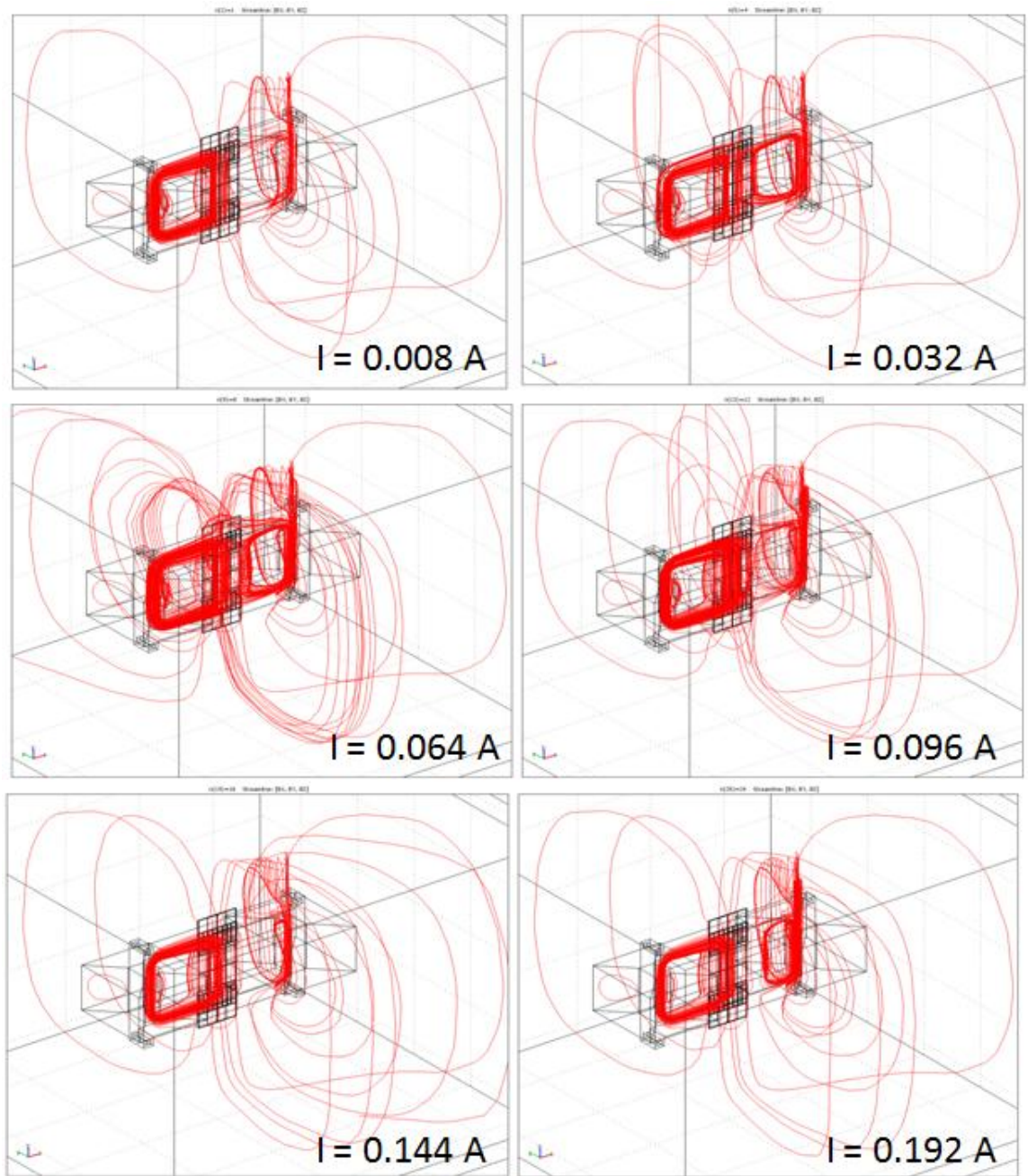


Figure 3.14: Simulated magnetic flux path of the transduction circuit for different coil currents

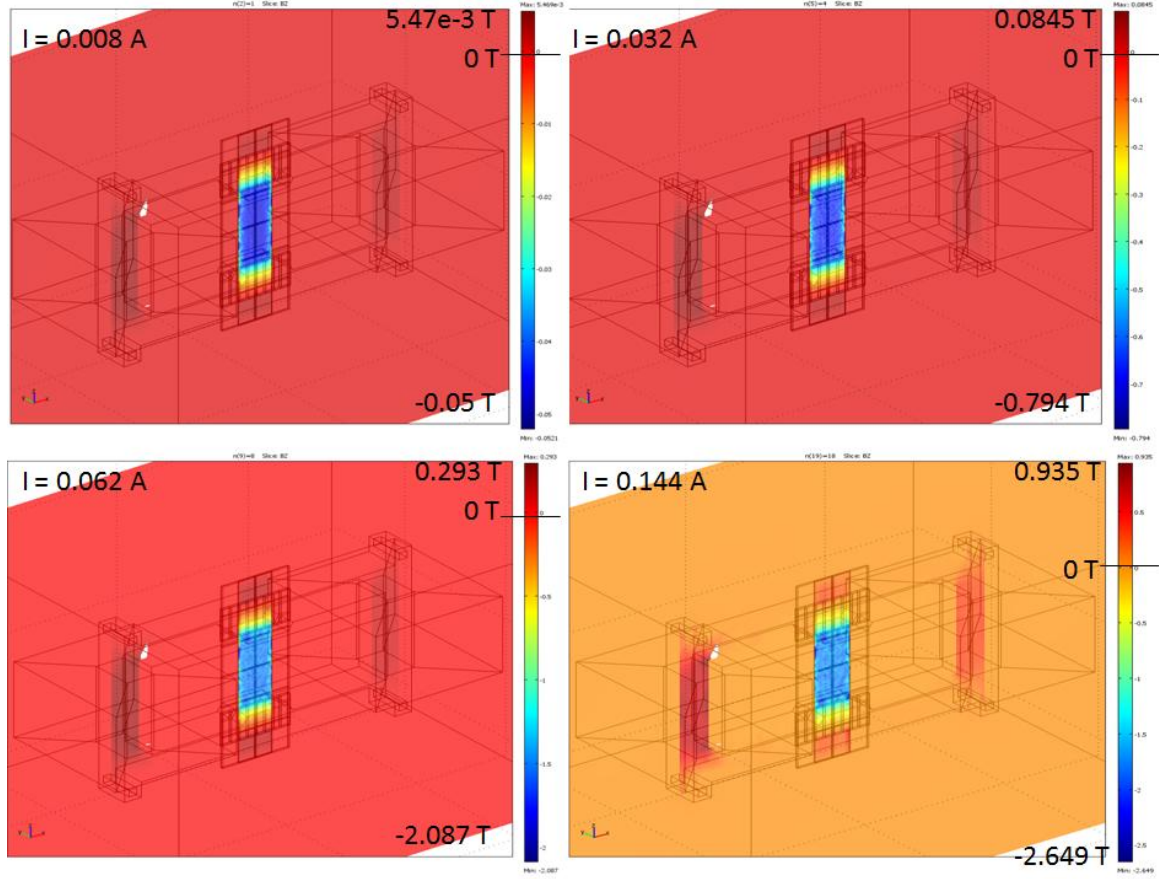


Figure 3.15: Simulated magnetic flux distribution through the mid plane of the Galfenol thickness

will likely lead to measurement errors and/or a decrease in actuation response. From simulation 4, the flux density distribution throughout the Galfenol was obtained, as shown in Figure 3.15. The flux density in the length direction of Galfenol is shown in slice plots (slice through mid plane of Galfenol thickness). For each plot, the current to the coils, the min and max flux density values, and the location of the zero value on the flux density scale are given.

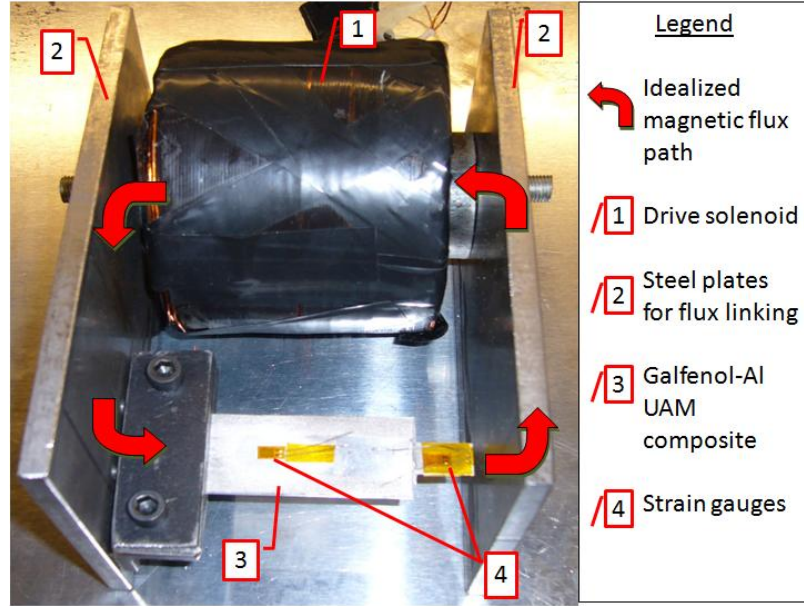


Figure 3.16: Test magnetic circuit for actuation testing

From Figure 3.15, it is seen that the magnetic flux is very uniform throughout the center of the Galfenol, where measurements will be taken. This consistency was always present while the Galfenol was magnetized from zero current.

3.3.3 Composite Actuation Modeling

3.3.3.1 Modeling of Test Magnetic Circuit

Before the magnetic transduction circuit was manufactured, a test magnetic circuit was created to obtain experimental data for actuation of the UAM composites. This circuit is shown in Figure 3.16. The Galfenol-aluminum composite used to obtain the experimental data was produced by Hahnlen [29], and is detailed in Figure 3.17.

Using the constitutive material model for Galfenol described in Section 3.3.1 and the material properties from Section 3.3.2, a 1:1 scale three-dimensional finite element model of the test magnetic circuit was developed. For increments in solenoid current,

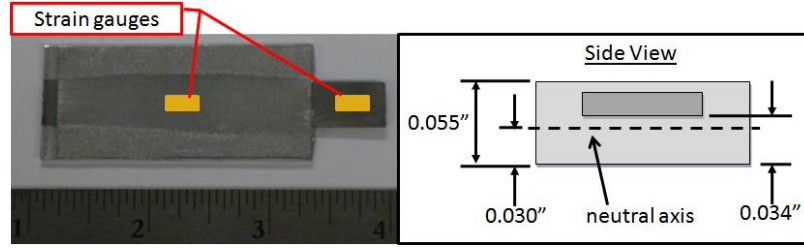


Figure 3.17: Galfenol-aluminum composite created using UAM [29]

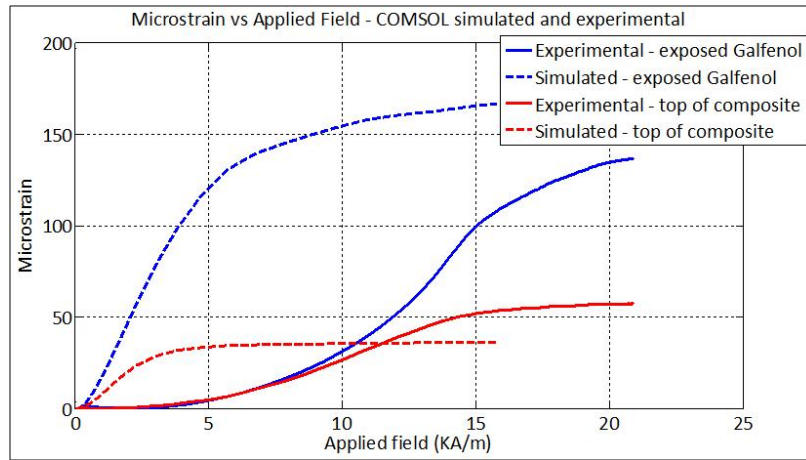


Figure 3.18: Simulated vs. experimental actuation of FeGa-Al UAM composite

the magnetic field strength, strain in the aluminum matrix of the composite, and strain in the Galfenol was measured. To compare with experimental data, the strain at the location of each strain gage was obtained by integrating the calculated strain (in the direction of the gage axis) over the contact area of each gage. The simulated strain response is compared to the experimental in Figure 3.18 for the first quarter of the major $\mathbf{S} - \mathbf{H}$ loop.

Large discrepancies exist between the simulated and experimental curves. The primary reason for this is the Galfenol material model itself. While the model can determine the spatially-dependent, nonlinear actuation and sensing curves, it requires experimentally determined characteristic curves to calculate the linear piezomagnetic coefficients. Typically, actuation and sensing curves for rolled Galfenol and Galfenol sheet do not exist (except for magnetostriction vs. magnetic field curves), due to the immaturity of the materials and continual improvements in their magnetomechanical responses. Sufficient experimental data for sheets of the EDM cut Galfenol steel does not exist. Thus, differences between the Galfenol steel response and the response of 18.4 at% highly-textured, polycrystalline Galfenol (used in the material model) will result in error. An actuation curve (magnetostriction vs. magnetic field) has been determined for the composite used in this simulation. This curve is reproduced in Figure 3.19 [29]. As shown in Figure 3.19, the EDM cut Galfenol steel that was exposed from the composite saturated at a magnetic field of ~ 22 kA/m with a magnetostriction of ~ 193 ppm. This saturation magnetostriction is in great disagreement with the experimental results obtained with the test magnetic circuit. Differences may be due to a misplaced or misaligned Hall probe or nonuniform magnetization of the exposed Galfenol during the experiments using the test magnetic circuit. Interestingly, the strain at the top of the composite is nearly identical in both cases (with differences likely attributed to the different boundary conditions for each experiment).

Both the simulated results of this research and the experimental results in [29] show that ~ 25 % of the magnetostriction available in the Galfenol can be transferred to the top surface of the composite. This result is present in both studies despite the difference in Galfenol materials used in the simulation compared to the experiment.

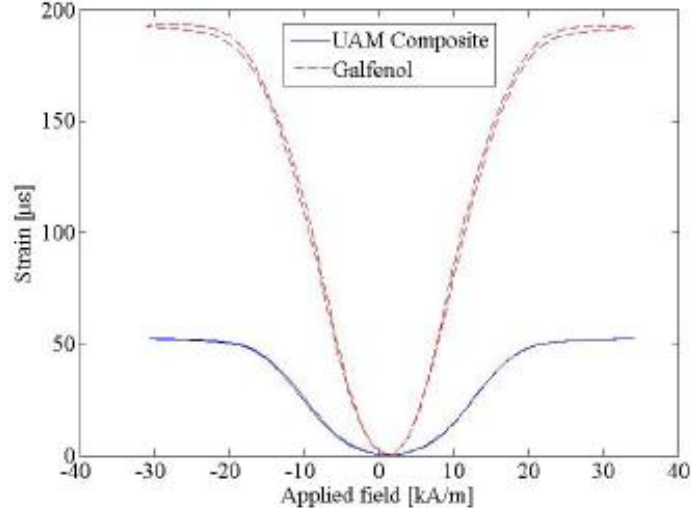


Figure 3.19: Experimental actuation of FeGa-Al UAM composite [29]

3.3.3.2 Model Parameters and Development

To estimate the actuation response of the composite, the model described in Section 3.3.2 was used. The mechanical response to the magnetic fields generated by the solenoids was obtained, in addition to the magnetic response, during the simulations in Section 3.3.2. Thus, the model description provided in said section suffices for this composite actuation simulation.

3.3.3.3 Results and Discussion

As shown earlier, the actuation response magnitudes calculated by the current Galfenol material model are incorrect, and require experimental characterization of the specific Galfenol material used. Despite, a simulation of the actuation response can show important trends and provide a basis upon which to assess the accuracy of experimental data, as discussed in Section 3.3.3.1. Figure 3.20, shows slice plots of

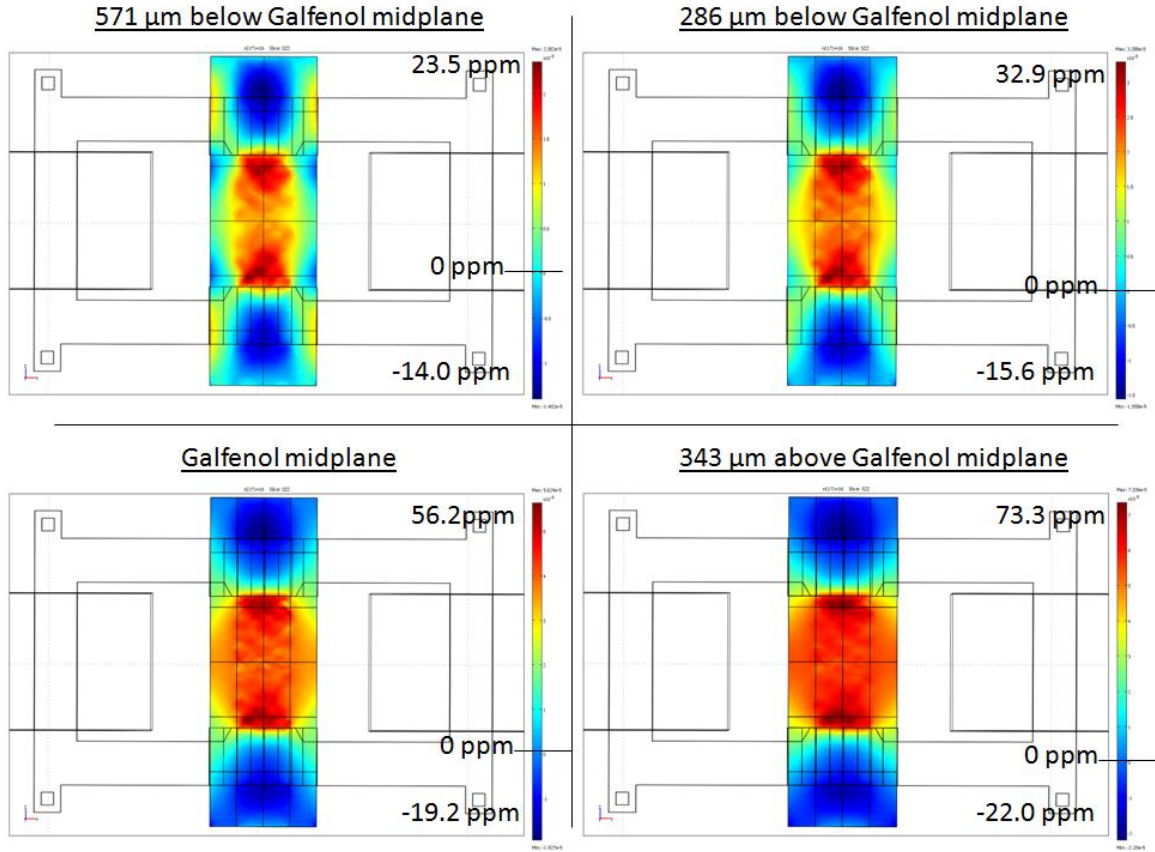


Figure 3.20: Simulated strain in UAM composite due to the saturated Galfenol actuation at solenoids currents of 0.128 A

strain (in the length direction of the Galfenol) for the mechanically active domains in the COMSOL simulation (in this case only the composite domains). The slice planes are in the Z-X plane (directions shown in Figure 3.12) and at varying distances away from the mid plane through the thickness of Galfenol. With reference to the schematic of the composite cross-section in Figure 2.5, the slice plane $571\text{ }\mu\text{m}$ (0.0225 in) below the Galfenol mid plane is essentially the bottom surface of the composite, and the slice plane $343\text{ }\mu\text{m}$ (0.0135 in) above the Galfenol mid plane is essentially the top surface of the composite.

In Figure 3.20, it can be seen that the strain in the composite increases from the plane furthest from the Galfenol to the mid plane of the Galfenol, and even up to the top surface of the composite, 343 μm (0.0135 in) above the Galfenol mid plane. This is due to the geometry of the composite, with Galfenol located above the neutral axis. Additionally, the loading of the Al matrix by the Galfenol actuation increases in the same fashion, as seen by the increase in size of the highly strained (red) region. Compression was generated in the Galfenol outside of the steel laminates, because of the fixed mechanical boundary condition shown in Figure 3.13 and the elongation of Galfenol between the steel laminate stacks.

CHAPTER 4

CONCLUSION

In this research, the prospect of embedding rolled Galfenol samples with wound induction coils was tested by embedding steel samples wound with induction coils. A 10.16 mm (0.4 in) wide steel sample, wound with a 60 turn induction coil was successfully embedded with two Al 3003-H18 foil using ultrasonic consolidation. Despite the embedding success, the induction coil was shorted to the Al matrix, although embedding was achieved with minimal deformation of the coil windings. It was theorized that a thicker insulation layer will provide increased protection during welding and will result in a reduction in the possibility of coil shorting.

From the rolled Galfenol steel embedding trials carried out, the importance of the contact pressure distribution, build geometry, and sample preparation was shown. Further, it was shown that a sample in which the Galfenol is flush with the surrounding aluminum before embedding will have difficulty embedding due to the difference in elastic modulus between Galfenol and the aluminum in the direction of the applied normal force. It was concluded that the failure to embed Galfenol into previously consolidated aluminum foils was likely due to the height to width ratio of the foils, which lead to excessive deflection of the foils during welding. Due to the success of embedding 0.4 in wide sheets of Galfenol in the literature and the lack of success of

embedding 0.5 in wide sheets in this research, despite the use of pressure-sensitive film and careful control of build geometry, it is theorized that a critical width of the active sample may exist, such that embedding samples wider is either impossible or very difficult.

A magnetic transduction circuit was manufactured with the ability to characterize sheets of Galfenol or thin composites containing magnetostrictive materials and to dynamically excite cantilevered composites or sheet material via frequency operation of coil current and/or cantilever beam base displacement. The design of the magnetic circuit was verified through a three-dimensional finite element simulation of the circuit magnetic response, with inclusion of the majority of the circuit complexities.

A test magnetic circuit was also manufactured to obtain experimental actuation curves for comparison with a three-dimensional finite element simulation. Comparisons showed discrepancies in the magnitude of the response, due to a lack of experimental data characterizing the Galfenol steel material. Despite, both the simulation and composite actuation curves in the literature showed that about 25 % of the available magnetostriction in the Galfenol samples could be transferred to the top surface of the composite, 0.006 in away from the embedded Galfenol.

The actuation response of the composite in the magnetic transduction circuit was also simulated. It was found that the magnetostriction of Galfenol is uniform in the region where measurements will be taken. Also, despite complete magnetization of the Galfenol in the composite, the magnetostriction of the embedded Galfenol only reached ~ 55 ppm, which is only 29 % of the saturation magnetostriction of the material itself. This, along with the strain developed in the Al matrix, shows significant loading of the Al encompassing the Galfenol. It was also determined from

the simulation, that the strain in the composite can exceed that in the embedded Galfenol for certain composite geometries in which the Galfenol is located away from the neutral axis.

Future work in this area should focus on perfecting the embedding of Galfenol into aluminum using UAM. Also, the critical width of the embedded active material should be investigated, and the width reported if it is shown to exist. The sensing response of the UAM composites that incorporate the EDM cut Galfenol sheet and rolled Galfenol should be obtained as a function of base excitation frequency using the cantilever beam vibration setup of the magnetic transduction circuit. These measurements should be supported by characterizing the Galfenol sheet and rolled Galfenol materials using the characterization setup of the magnetic circuit.

BIBLIOGRAPHY

- [1] AKSteel. Oriented and trans-oriented electrical steels product data bulletin. Technical report, 2011.
- [2] W.D. Armstrong. Magnetization and magnetostriction processes in $\text{Fe}_{0.27-0.30}\text{Co}_{0.73-0.70}$. *Journal of Applied Physics*, 81(5):2321–2326, 1997.
- [3] Material Database AZoM. Transducer materials for sonar systems - materials comparison [available online], 2002.
- [4] O.W. Bertacchini, D.C. Lagoudas, F.T. Calkins, and J.H. Mabe. Thermomechanical cyclic loading and fatigue life characterization of nickel rich nitinol shape-memory alloy actuators. In *Proceedings of SPIE*, volume 6929, page 692916, 2008.
- [5] S. Chakrabarti and M. Dapino. 3d dynamic finite element model for magnetostrictive galenol-based devices. In *Proceedings of SPIE*, volume 7978, page 79781C, 2011.
- [6] S. Chakrabarti and M.J. Dapino. A dynamic model for a displacement amplified magnetostrictive driver for active mounts. *Smart Materials and Structures*, 19:055009, 2010.
- [7] L.M. Cheng and E. Summers. Texture development in polycrystalline Fe-Ga magnetostrictive materials. In *Materials science forum*, volume 539, pages 3460–3465. Trans Tech Publ, 2007.
- [8] A. Clark. *Magnetostrictive Rare Earth-Fe₂ Compounds*, volume 1, chapter 7 in *Ferromagnetic Materials*, page 531. North Holland Publ. Co., 1980.
- [9] A. Clark, M. Wun-Fogle, J. Restorff, and T. Lograsso. Magnetostrictive properties of galenol alloys under compressive stress. *Materials Transactions - JIM*, 43:881–886, 2002.

- [10] AE Clark, KB Hathaway, M. Wun-Fogle, JB Restorff, TA Lograsso, VM Kepsens, G. Petculescu, and RA Taylor. Extraordinary magnetoelasticity and lattice softening in bcc fe-ga alloys. *Journal of applied physics*, 93(10):8621–8623, 2003.
- [11] J.A. Collins, H.R. Busby, and G.H. Staab. *Mechanical Design of Machine Elements and Machines*. Wiley, 2009.
- [12] M.J. Dapino, R.C. Smith, F.T. Calkins, and A.B. Flatau. A coupled magnetomechanical model for magnetostrictive transducers and its application to villari-effect sensors. *Journal of intelligent material systems and structures*, 13(11):737, 2002.
- [13] S. Datta, J. Atulasimha, C. Mudivarthi, and AB Flatau. The modeling of magnetomechanical sensors in laminated structures. *Smart Materials and Structures*, 17:025010, 2008.
- [14] S. Datta, J. Atulasimha, C. Mudivarthi, and A.B. Flatau. Modeling of magnetomechanical actuators in laminated structures. *Journal of Intelligent Material Systems and Structures*, 20(9):1121, 2009.
- [15] E. De Vries. *Mechanics and Mechanisms of Ultrasonic Metal Welding*. PhD thesis, The Ohio State University, 2004.
- [16] RR Dehoff and SS Babu. Characterization of interfacial microstructures in 3003 aluminum alloy blocks fabricated by ultrasonic additive manufacturing. *Acta Materialia*, 58(13):4305–4315, 2010.
- [17] G. Engdahl. *Handbook of Giant Magnetostrictive Materials*. Academic Pr, 2000.
- [18] Inc. ETREMA Products. Material safety data sheet for etrema galfenol material. Technical report, 2010.
- [19] Inc. ETREMA Products. Terfenol-d product information and product literature [available online]. Technical report, 2011.
- [20] P. Evans. *Nonlinear Magnetomechanical Modeling and Characterization of Galfenol and System-Level Modeling of Galfenol-Based Transducers*. PhD thesis, The Ohio State University, 2009.
- [21] P. Evans and M. Dapino. Efficient magnetic hysteresis model for field and stress application in magnetostrictive galfenol. *Journal of Applied Physics*, 107(6):063906–063906, 2010.
- [22] P. Evans and M. Dapino. Dynamic model for 3-d magnetostrictive transducers. *Magnetics, IEEE Transactions on*, 47(1):221–230, 2011.

- [23] D.A. Fleisch. *A Student's Guide to Maxwell's Equations*. Cambridge Univ Press, 2008.
- [24] M. Gandhi and B. Thompson. *Smart Materials and Structures*. Chapman and Hall, 1992.
- [25] B. Goldsmith, E. Foyt, and M. Hariharan. The role of offshore monitoring in an effective deepwater riser integrity management program. In *26th International Conference on Offshore Mechanics and Arctic Engineering*. OMAE, 2007.
- [26] R. Hahnlen. Development and characterization of niti joining methods and metal matrix composite transducers with embedded niti by ultrasonic consolidation. Master's thesis, The Ohio State University, 2009.
- [27] R. Hahnlen. Multifunctional composites with embedded sensing. In *Smart Vehicle Concepts Center (SVC) conference presentation*, February 2010.
- [28] R. Hahnlen, M. Dapino, M. Short, and K. Graff. Aluminum-matrix composites with embedded ni-ti wires by ultrasonic consolidation. In *Proceedings of SPIE*, volume 7290, page 729009, 2009.
- [29] R. Hahnlen and M.J. Dapino. Active metal-matrix composites with embedded smart materials by ultrasonic additive manufacturing. In *Proceedings of SPIE*, volume 7645, page 76450O, 2010.
- [30] C. Hopkins. Development and characterization of optimum process parameters for metallic composites made by ultrasonic consolidation. Master's thesis, The Ohio State University, 2010.
- [31] D. Jiles. *Introduction to magnetism and magnetic materials*. CRC, 1998.
- [32] K. Johnson. *Interlaminar Subgrain Refinement in Ultrasonic Consolidation*. PhD thesis, Loughborough University, Loughborough, UK, 2008.
- [33] R. Kellogg. *Development and Modeling of Iron-Gallium Alloys*. PhD thesis, Iowa State University, 2003.
- [34] R. Kellogg, A. Flatau, A. Clark, M. Wun-Fogle, and T. Lograsso. Temperature and stress dependencies of the magnetic and magnetostrictive properties of fe_{0.81}ga_{0.19}. *Journal of applied physics*, 91(10):7821–7823, 2002.
- [35] R. Kellogg, A. Flatau, A. Clark, M. Wun-Fogle, and T. Lograsso. Texture and grain morphology dependencies of saturation mmagnetostriction in rolled polycrystalline fe₈₃ga₁₇. *Journal of applied physics*, 93(10):8495–8497, 2003.

- [36] R. Kellogg, A. Russell, T. Lograsso, A. Flatau, A. Clark, and M. Wun-Fogle. Tensile properties of magnetostrictive iron-gallium alloys. *Acta materialia*, 52(17):5043–5050, 2004.
- [37] CY Kong and RC Soar. Fabrication of metal-matrix composites and adaptive composites using ultrasonic consolidation process. *Materials Science and Engineering: A*, 412(1-2):12–18, 2005.
- [38] CY Kong, RC Soar, and PM Dickens. Characterisation of aluminium alloy 6061 for the ultrasonic consolidation process. *Materials Science and Engineering A*, 363(1-2):99–106, 2003.
- [39] CY Kong, RC Soar, and PM Dickens. Optimum process parameters for ultrasonic consolidation of 3003 aluminium. *Journal of materials processing technology*, 146(2):181–187, 2004.
- [40] CY Kong, RC Soar, and P.M. Dickens. A model for weld strength in ultrasonically consolidated components. *Proceedings of the Institution of Mechanical Engineers, Part C: Journal of Mechanical Engineering Science*, 219(1):83–91, 2005.
- [41] M. Kulakov and H. Rack. Control of 3003-h18 aluminum ultrasonic consolidation. *Journal of Engineering Materials and Technology*, 131:021006, 2009.
- [42] D. Li and R. Soar. Influence of sonotrode texture on the performance of an ultrasonic consolidation machine and the interfacial bond strength. *Journal of Materials Processing Technology*, 209(4):1627–1634, 2009.
- [43] T.K. Lim, S. Natarajan, and P. An. Mid-water flowline integrity monitoring strategy. In *29th International Conference on Ocean, Offshore and Arctic Engineering*. ASME, 2010.
- [44] X. Liu, S. Zhang, J. Luo, TR Shrout, and W. Cao. A complete set of material properties of single domain 0.26 pb (in [sub 1/2] nb [sub 1/2]) o [sub 3]–0.46 pb (mg [sub 1/3] nb [sub 2/3]) o [sub 3]–0.28 pbtio [sub 3] single crystals. *Applied Physics Letters*, 96:012907, 2010.
- [45] A. Mahadevan. Force and torque sensing with galphenol alloys. Master’s thesis, The Ohio State University, 2009.
- [46] SAES Smart Materials. Nitinol data [available online]. Technical report, 2009.
- [47] R. Meloy and E. Summers. Magnetic property-texture relationships in galphenol rolled sheet stacks. *Journal of Applied Physics*, 109:07A930, 2011.

- [48] Inc. Metglas. Powerlite c-cores technical bulletin [available online]. Technical report, 2011.
- [49] Pulse Structural Monitoring. Steel catenary riser monitoring product literature [available online].
- [50] C. Mou, P. Saffari, D. Li, K. Zhou, L. Zhang, R. Soar, and I. Bennion. Smart structure sensors based on embedded fibre bragg grating arrays in aluminium alloy matrix by ultrasonic consolidation. *Measurement Science and Technology*, 20:034013, 2009.
- [51] S. Na and A. Flatau. Secondary recrystallization, crystallographic texture and magnetostriction in rolled fe-ga based alloys. *Journal of applied physics*, 101(9):09N518–09N518, 2007.
- [52] S.M. Na and A.B. Flatau. Magnetostriction and crystallographic texture in rolled and annealed fe-ga based alloys. *Materials and Devices for Smart Systems II*, 888:335–340, 2005.
- [53] S.M. Na and A.B. Flatau. Deformation behavior and magnetostriction of polycrystalline fe-ga-x (x= b, c, mn, mo, nb, nbc) alloys. *Journal of Applied Physics*, 103:07D304, 2008.
- [54] M. Norfolk, M. Short, and K. Graff. A very high-power ultrasonic additive manufacturing system for advanced materials. In *International Conference on Additive Manufacturing*, 2010.
- [55] R O’Handley, J. Huang, D. Bono, and J. Simon. Improved wireless, transcutaneous power transmission for in vivo applications. *IEEE Sensors Journal*, 8(1), 2008.
- [56] AR Pelton, V. Schroeder, MR Mitchell, X.Y. Gong, M. Barney, and SW Robertson. Fatigue and durability of nitinol stents. *Journal of the Mechanical Behavior of Biomedical Materials*, 1(2):153–164, 2008.
- [57] G.D.J. Ram, Y. Yang, and BE Stucker. Effect of process parameters on bond formation during ultrasonic consolidation of aluminum alloy 3003. *Journal of Manufacturing Systems*, 25(3):221, 2006.
- [58] JB Restorff and M. Wun-Fogle. Temperature dependence of the magnetostriction of stress annealed galfenol measured under tension. *Journal of Applied Physics*, 107(9):09A913–09A913, 2010.
- [59] CJ Robinson, C. Zhang, G.D.J. Ram, E.J. Siggard, B. Stucker, and L. Li. Maximum height to width ratio of freestanding structures built using ultrasonic consolidation. In *Solid Freeform Fabrication Symposium*, pages 502–516, 2007.

- [60] E.J. Siggard, A.S. Madhusoodanan, B. Stucker, and B. Eames. Structurally embedded electrical systems using ultrasonic consolidation (uc). In *Proceedings of the 17th Solid Freeform Fabrication Symposium, Austin, Texas, USA, August, 2006*.
- [61] K. Sojiphan, M. Sriraman, and S. Babu. Stability of microstructure in al3003 builds made by very high power ultrasonic additive manufacturing. In *Twenty Second Annual International Solid Freeform Fabrication Symposium An Additive Manufacturing Conference*, 2010.
- [62] WB Spillman Jr, JS Sirkis, and PT Gardiner. Smart materials and structures: What are they? *Smart Material Structures*, 5:247–254, 1996.
- [63] N. Srisukhumbowornchai and S. Guruswamy. Crystallographic textures in rolled and annealed fe-ga and fe-al alloys. *Metallurgical and Materials Transactions A*, 35(9):2963–2970, 2004.
- [64] E. Summers, M. Brooks, and T. Lograsso. Gallium content effects in low carbon steels. In *Materials Science & Technology 2009 Conference and Exhibition*, pages 1442–1453, 2009.
- [65] E. Summers, T. Lograsso, and M. Wun-Fogle. Magnetostriction of binary and ternary fe-ga alloys. *Journal of Materials Science*, 42(23):9582–9594, 2007.
- [66] E. Summers, R. Meloy, and S. Na. Magnetostriction and texture relationships in annealed galfenol alloys. *Journal of Applied Physics*, 105(7):07A922–07A922, 2009.
- [67] E. Summers, R. Meloy, and JB Restorff. Galfenol alloying additions and the effects on uniaxial anisotropy generation. *Journal of Applied Physics*, 106(2):024914–024914, 2009.
- [68] G. Thivend and N. Murray. Subsea sensors for non-intrusive monitoring of temperature, pressure and asset integrity. In *Offshore Technology Conference*, pages 20980–MS, 2010.
- [69] S. Tumanski. Induction Coil Sensors a Review. *Measurement Science and Technology*, 18:R31, 2007.
- [70] M. Wun-Fogle, JB Restorff, and AE Clark. Magnetostriction of stress-annealed fe-ga and fe-ga-al alloys under compressive and tensile stress. *Journal of intelligent material systems and structures*, 17(2):117, 2006.
- [71] M. Wun-Fogle, JB Restorff, AE Clark, E. Dreyer, and E. Summers. Stress annealing of fe-ga transduction alloys for operation under tension and compression. *Journal of applied physics*, 97(10):10M301–10M301, 2005.

- [72] Q. Xing, Y. Du, RJ McQueeney, and TA Lograsso. Structural investigations of fe-ga alloys: Phase relations and magnetostrictive behavior. *Acta Materialia*, 56(16):4536–4546, 2008.
- [73] J. Yoo, S. Na, J. Restorff, M. Wun-Fogle, and A. Flatau. The effect of field annealing on highly textured polycrystalline galphenol strips. *Magnetics, IEEE Transactions on*, 45(10):4145–4148, 2009.
- [74] J. Yoo, J. Restorff, M. Wun-Fogle, and A. Flatau. The effect of magnetic field annealing on single crystal iron gallium alloy. *Journal of Applied Physics*, 103:07B325, 2008.
- [75] J. Yoo, J. Restorff, M. Wun-Fogle, and A. Flatau. Induced magnetic anisotropy in stress-annealed galphenol laminated rods. *Smart Materials and Structures*, 18:104004, 2009.
- [76] J.H. Yoo and A.B. Flatau. Measurement of field-dependence elastic modulus of iron-gallium alloy using tensile test. *Journal of applied physics*, 97:10M318, 2005.
- [77] J. Zhai, Z. Xing, S. Dong, J. Li, and D. Viehland. Magnetoelectric laminate composites: An overview. *Journal of the American Ceramic Society*, 91(2):351–358, 2008.